

The GAPS programme at TNG

? TOI-1533: a compact system hosting a super-Neptune-mass pair with disparate radii

G. Mantovan^{1,2}, V. Nascimbeni², S. Desidera², L. Malavolta^{3,2}, J. J. Lissauer⁴, P. Leonardi^{3,2}, T. Azevedo Silva⁵, C. Guerra⁶, D. Polychroni⁷, L. Borsato², M. Baratella⁸, K. Biazzo⁹, D. Nardiello^{3,2}, K. A. Collins¹⁰, M. Damasso¹¹, J. De Leon¹², M. E. Everett¹³, D. Gandolfi¹⁴, S. Giacalone¹⁵, L. Naponiello¹¹, G. Piotto^{3,2}, G. Scandariato¹⁶, K. Stassun¹⁷, S. W. Yee^{18,*}, L. Affer⁶, F. Amadori¹¹, A. Bignamini⁷, S. Colombo⁶, M. D’Arpa⁶, C. D. Dressing¹⁹, A. Fukui^{12,20}, A. Ghedina²¹, J. Higuera¹³, K. Ikuta²², Kawauchi²³, J. Korth^{24,20,25}, V. Lorenzi²¹, L. Mancini^{26,11,27}, M. Mori^{28,29}, F. Murgas^{20,25}, N. Narita^{12,28,20}, E. Palle^{20,25}, H. Parviainen^{20,25}, A. Ruggieri², A. Savel³⁰, R. P. Schwarz¹⁰, A. Shporer³¹, G. Srdoc³², Stockdale³³, D. Watanabe³⁴, R. Zambelli³⁵, and T. Zingales^{3,2}

(Affiliations can be found after the references)

Compiled: July 1, 2026

ABSTRACT

The present-day architecture of planetary systems contains information about their formation and migration histories. The origin of hot Jupiters (HJs, $P \lesssim 10$ d, $R_p > 8R_\oplus$) has long been a matter of debate. While most of them are found to be “lonely”, there is a rare population of HJs hosting small companions on inner orbits (eight known as of May 2026). Their peculiar architecture suggests a gentle disc-migration mechanism. In this study, we present the discovery and characterisation of the multi-planet system TOI-1533, comprising an inner sub-Neptune (TOI-1533 b, $P_{\text{orb}} = 3.63$ d, $R_p = 3.15 R_\oplus$) and an outer hot giant planet (TOI-1533 c, $P_{\text{orb}} = 8.06$ d, $R_p > 7.5 R_\oplus$) with substantial H/He by mass ($\rho_p < 0.48$ g cm⁻³), both transiting an active K-dwarf star ($T_{\text{eff}} \approx 5130$ K; V (mag) ≈ 11). Our joint modelling of stellar activity and planetary signals from radial velocities (HARPS-N) and transits (TESS) allows us to detect their Keplerian signals (approximately 10σ) and to isolate the stellar modulation. The inclusion of simultaneous photometry in the multi-dimensional Gaussian processes formalism was a fundamental addition to the spectroscopic activity indicators, enabling the disentanglement of stellar activity from planetary signals. The mass ratio of the two confirmed planets (M_b/M_c about 0.8), together with the super-Neptune mass of the large outer companion ($M_c \approx 40M_\oplus$), makes this system unusual compared to the other few HJs with low-mass inner companions.

Key words. Planets and satellites: fundamental parameters – Stars: fundamental parameters – Planets and satellites: gaseous planets

1. Introduction

The origin of gas giants on close-in orbits ($P \lesssim 10$ d, $R_p > 8R_\oplus$), known as hot Jupiters (HJs), is a long-standing question in planet formation and evolution theories. Although many scenarios have been proposed to place HJs in their current orbits (e.g. disc-migration, high-eccentricity migration), none can satisfy all the observational constraints (Dawson & Johnson 2018). The answer seems hidden in the architectures of their systems, which remain only partially understood. One clue is that HJs are typically “lonely” and their companions, if present, are often massive and on wide orbits ($P > 200$ d, Schlaufman & Winn 2016).

The lack of small, low-mass, short-period companions initially suggested that HJs form beyond the snow line and then migrate inwards via high-eccentricity migration (HEM, Wu & Murray 2003). In this scenario, the eccentricity of a gas giant is excited by close encounters with other giant planets (e.g. Rasio & Ford 1996) or by Kozai’s interaction with a distant stellar companion (Eggleton & Kiseleva-Eggleton 2001). If the periastron distance is small enough, the orbit circularises and shrinks due to star-planet tidal interaction. Such dynamical instability is destructive for low-mass bodies in the path of the

migrating giant (Mustill et al. 2015), inevitably leaving HJs in loneliness. However, among the 500+ known HJs, a growing number of exceptions host low-mass inner companions. These are WASP-47 (Becker et al. 2015), Kepler-730 (Cañas et al. 2019), TOI-1130 (Huang et al. 2020), WASP-132 (Hord et al. 2022), TOI-2000 (Sha et al. 2023), TOI-5398 (Mantovan et al. 2022, 2024a), TOI-1408 (Korth et al. 2024), and TOI-5143 (Quinn et al. 2026). Their peculiar architecture suggests an alternative, gentler migration mechanism.

Under disc migration, tidal interactions with the protoplanetary disc move the initially cold giant inward from its birthplace (Lin et al. 1996), sweeping material along its mean-motion resonances to form inner planets (Raymond et al. 2006). Measuring the occurrence rate of these inner companions can help determine the fraction of HJs that formed via disc migration versus HEM (Sha et al. 2023). Precise masses and orbital parameters are needed to study the formation and migration scenarios of these maverick systems (e.g., Serrano et al. 2022). At present, however, the sample of systems with companions is too small and relatively uncharacterised to answer this question.

In this work, we present the discovery and characterisation of a new system of this kind, TOI-1533. All the data and observations collected for this purpose are described in Sect. 2, while we describe TOI-1533's stellar properties in Sect. 3. We present our joint modelling of the photometric and spectroscopic data used to confirm both planets in Sect. 4. Section 5 discusses our results and presents the specific and global characteristics of this new multi-planet system comprising a super-Neptune-mass pair with disparate radii. Concluding remarks are reported in Sect. 6.

2. Observations and data reduction

2.1. TESS photometry

The planetary system presented in this work was first detected in TESS photometry (TOI-1533.01, $P \approx 3.6$ d; TOI-1533.02, $P \approx 8.1$ d). In particular, TESS observed TOI-1533 (TIC 345143460) at 30 min cadence in Sectors 17 and 24, at 2 min cadence in Sectors 57, 77, 78, 84, and 85.

We extracted TESS lightcurves following the PATHOS approach (see Nardiello et al. 2020, for a thorough description), which also allowed us to minimise neighbour flux contamination (see e.g. Nardiello et al. 2022; Mantovan et al. 2024a).

2.2. ASAS-SN photometry

We inspected almost 6 years of archival data from ASAS-SN (Shappee et al. 2014; Kochanek et al. 2017), with observations spanning from June 2019 to November 2024, to estimate the stellar rotation period (see Sect. 3.4). The data for TOI-1533 were taken in the Sloan g -band and consist of images with a resolution of 8 arcsec/pixel ($\sim 15''$ FWHM PSF).

2.3. Planets vetting and validation

This subsection presents the data aimed at demonstrating that both candidates (TOI-1533.01, TOI-1533.02) in the system are high-confidence planets (from now on TOI-1533 b, TOI-1533 c), with multiple uncontaminated ground-based observations as part of the TESS Follow-up Observing Program (Sub Group 1, TFOP Collins 2019)¹ detecting both planets and excluding deep, false-positive eclipses. We used the TESS Transit Finder, a customised version of the Tapir software package (Jensen 2013), to schedule our follow-up transit observations. Moreover, recon spectroscopic analyses rule out the presence of a spectroscopic binary. The data are analysed and presented later in Sect. 4.

2.3.1. LCOGT

We observed full transit windows of TOI-1533 b in Pan-STARRS z_s band on UT 2023 December 3, 2024 August 4, 2024 August 11 from the Las Cumbres Observatory Global Telescope (LCOGT; Brown et al. 2013) 1.0 m network nodes at Teide Observatory on the island of Tenerife (Teide), and McDonald Observatory near Fort Davis, Texas, United States (McD), respectively. We observed a full transit window of TOI-1533 c in Sloan i' band on UT 2023 October 7 from the LCOGT 0.35 m network node at Haleakala Observatory on Maui, Hawai'i (Hal). We also observed full transit windows of TOI-1533 c on UT 2024 October 12 and 2025 November 3 from the LCOGT 2.0 m Faulkes Telescope North at Haleakala Observatory. The Faulkes Telescope North is equipped with the MuSCAT3 multi-band imager

(Narita et al. 2020). All images were calibrated with BANZAI (McCully et al. 2018), and photometric data were extracted using AstroImageJ (Collins et al. 2017). Circular apertures with 4–8'' radii were used to extract the differential photometry. All apertures excluded flux from the nearest Gaia DR3 star (Gaia DR3 1998672965462506496), which is 13'' southwest of TOI-1533, confirming both transit signals on target. MuSCAT3 observations across Sloan g' , r' , i' , and z_s bands show no indication of transit depth chromaticity in TOI-1533 c transits. All lightcurves are included in the joint modelling described in sect. 4.1.

2.3.2. MuSCAT2

We observed two full transits of TOI-1533 b on 2023-11-11 and 2024-09-23 UT under variable weather conditions, with intermittent cloud passages, and one full transit of TOI-1533 c on 2023-12-26 under clear conditions. The observations were obtained in the g' , r' , i' , and z_s bands using the MuSCAT2 (Narita et al. 2019) instrument mounted on the 1.52 m TCS telescope at Teide Observatory in the Canary Islands, Spain. Exposure times ranged from 5 to 15 s depending on observing conditions. A slight telescope defocus was applied to improve photometric precision while maintaining the resolution of a nearby star located 13'' from the target.

Data reduction and aperture photometry were performed using the MuSCAT2 pipeline², described in Parviainen et al. (2020). The pipeline evaluates multiple combinations of comparison stars and aperture radii. Optimal light curves were selected through a global optimisation procedure that fits a model including the five brightest comparison stars within the field of view and uncontaminated photometric apertures. We could only marginally detect the TOI-1533 b transit due to unfavourable weather, whereas we detected an on-time and achromatic transit of TOI-1533 c with high significance.

2.3.3. Adaptive optics imaging

We observed TOI-1533 on UT 2020 December 1 using the ShARCS camera on the Shane 3-meter telescope at Lick Observatory (Kupke et al. 2012; Gavel et al. 2014; McGurk et al. 2014). Observations were taken with the Shane adaptive optics system in natural guide star mode to search for nearby, unresolved stellar companions. We collected a single sequence of observations using a K_s filter ($\lambda_0 = 2.150 \mu\text{m}$, $\Delta\lambda = 0.320 \mu\text{m}$). We reduced the data using the publicly available SIMMER pipeline (Savel et al. 2020).³ Our reduced images and corresponding contrast curves are shown in Fig. F.7. Our observations achieved a contrast of 3.0 at 0.5'' and 4.5 at 1.0''. We found no nearby stellar companions within our detection limits.

2.3.4. Speckle imaging

We observed TOI-1533 on UT 2022 September 17 using the NN-EXPLORE Exoplanet Stellar Speckle Imager (NESSI; Scott et al. 2018), a speckle imager at the WIYN 3.5 m telescope on Kitt Peak. The data consist of 7000 40 ms frames in two filters with central wavelengths $\lambda_c = 562$ and 832 nm. NESSI's FOV was confined to a 256×256 pixel sub-array readout (4.6''×4.6''). However, our speckle measurements were further restricted to an outer radius of 1.2'' from the target star. A similar set of 1000

¹ <https://tess.mit.edu/followup>

² https://github.com/hparvi/MuSCAT2_transit_pipeline

³ <https://github.com/arjunsavel/SIMMER>

speckle frames was taken of a nearby, single star in order to calibrate the PSF of the TOI-1533 data.

These speckle data were reduced following Howell et al. (2011). We obtained a contrast curve from each reconstructed image of the field by measuring fluctuations in the noise-like background level as a function of separation from TOI-1533 (Fig. F.8). These contrast curves establish the upper limits on the relative brightness of any undetected point source in proximity to the target star. No companion sources were detected for TOI-1533 in the NESSI data.

2.3.5. Reconnaissance spectroscopy

TOI-1533 was observed with the HIRES (High Resolution Echelle Spectrometer Howard et al. 2010) spectrograph mounted on the Keck telescope as part of the California Planet Survey (CPS) between December 2019 and June 2020. These observations confirm the absence of any sign of a spectroscopic binary down to a flux ratio of 1%, and demonstrate that the star is quite active, with an S-index value from the highest SNR spectrum of 0.432 ± 0.05 (Isaacson et al. 2024) and $\log R'_{\text{HK}} = -4.57 \pm 0.06$, using $(B - V)_0$ from Table 1. TRES echelle spectrograph (Szentgyorgyi & Furész 2007) observations spread out over two years show a downward drift of about 200 m s^{-1} , but also exclude any sign of a false positive scenario.

2.4. HARPS-N spectroscopic follow-up

We observed TOI-1533 with the High Accuracy Radial velocity Planet Searcher for the Northern hemisphere (HARPS-N; Cosentino et al. 2012) spectrograph at TNG between October and December 2024, obtaining a total of 17 spectra with 1200 s of exposure time, average S/N of 44 at 5500 \AA and spanning a time window of 82 days. It is worth noting that *TESS* sectors 84 and 85 overlap with the spectroscopic observations. The spectra, which cover the wavelength range $383 - 693 \text{ nm}$ and have a resolving power of $\approx 115\,000$, have been collected under the open-time proposal A50TAC_30 (PI: G. Mantovan). We agreed to share the awarded time with other Global Architecture of Planetary Systems (GAPS, Covino et al. 2013) programs requesting RV monitoring, to ensure the optimisation and coordination of the observations.

The HARPS-N RV data reduction was carried out in a way similar to that presented in several previous GAPS papers. In particular, we used the HARPS-N DRS v3.2.0, derived from the ESPRESSO DRS (Dumusque et al. 2021), and computed the RVs using the cross-correlation function (CCF) method (Pepe et al. 2002) with a G9 mask. To better distinguish the activity contribution from the Keplerian signals in the RV dataset, we additionally extracted multiple activity indicators. Specifically, from the HARPS-N DRS we extracted the value of the CCF bisector span (BIS), the full width at half-maximum (FWHM) and its equivalent width (W_{CCF} Malavolta et al. 2017; Collier Cameron et al. 2019). The chromospheric $\log R'_{\text{HK}}$ index was instead obtained using a method from Lovis et al. (2011) available on the YABI workflow interface (Hunter et al. 2012), installed at the IA2 data center⁴.

2.5. NEID spectroscopic follow-up

We observed TOI-1533 with the NEID spectrograph (Schwab et al. 2016; Halverson et al. 2016) on the WIYN

3.5m telescope at Kitt Peak National Observatory (KPNO). We obtained seven spectra between 2025-07-10 and 2025-10-31 in high-resolution (HR) mode ($R \sim 110,000$), with exposure times of 480s, attaining S/N of 25–35 at 5500 \AA . The data were reduced using v1.4.2 of the standard NEID Data Reduction Pipeline (DRP),⁵ with precise RVs extracted by cross-correlating the spectrum with a weighted stellar line mask for spectral type K2 (Baranne et al. 1996; Pepe et al. 2002). Stellar activity indicators were also extracted from each spectrum using the standard DRP algorithms.

3. Stellar parameters

We determined TOI-1533 stellar parameters using photometric, astrometric, spectroscopic and further ancillary data. The whole procedure starts by producing a co-added spectrum using all the HARPS-N spectra, with an average S/N of ~ 230 per extracted pixel at around 6000 \AA .

3.1. Atmospheric parameters and iron abundance

We analysed the co-added HARPS-N spectrum to derive the effective temperature T_{eff} , the surface gravity $\log g$, the iron abundance $[\text{Fe}/\text{H}]$, and the microturbulence velocity ξ following the same methodology as in Basilicata et al. (2025). We employed the standard equivalent width (EW) method with Fe I and Fe II lines from the Biazzo et al. (2022) list. Briefly, we measured EWs with the automatic tool ARES (v2, Sousa et al. 2015) and by using the qoyllur-quipu software (q2⁶, Ramírez et al. 2014). The 1D-LTE model atmospheres with new opacities from the Castelli & Kurucz (2003) grid have been adopted. The final values of the spectroscopic stellar parameters can be found in Table 1, suggesting a K1 type dwarf (from Pecaat & Mamajek 2013, version 2022.04.16) with super-solar chemical composition. Our final value of $T_{\text{eff,spec}}$ agrees perfectly with the estimates obtained with the *colte* tool (Casagrande et al. 2021) with various colour-indexes using 2MASS (Cutri et al. 2003) and *Gaia*-DR3 (Gaia Collaboration et al. 2023) photometry. The mean photometric value of $T_{\text{eff,phot}}$ is $5127 \pm 73 \text{ K}$, spanning from a minimum in $(G - B_p)$ of $5023 \pm 54 \text{ K}$ and a maximum in $(R_p - H)$ of $5238 \pm 72 \text{ K}$. The spectroscopic $\log g$ is also in perfect agreement with the value reported in the *Gaia* catalogue of 4.53 ± 0.03 . Finally, the microturbulence velocity we obtained is comparable within the uncertainties to the value of $0.80 \pm 0.05 \text{ km s}^{-1}$ measured via the empirical relation of (Dutra-Ferreira et al. 2016).

3.2. Infrared flux method and isochrones

We derived the stellar radius and mass of TOI-1533 from its atmospheric parameters (T_{eff} , $\log g$) using a custom-built code that combines the infrared flux method (IRFM, Blackwell & Shallis 1977; Stassun et al. 2017) and isochrone fitting (MCMCI code, Bonfanti & Gillon 2020). The process is fully described, for example, in Bonfanti et al. (2026) and Mantovan et al. (2026). The resulting values are reported in Table 1. Stellar atmospheric models were taken from the ATLAS catalogues (Castelli & Kurucz 2003).

⁵ <https://neid.ipac.caltech.edu/docs/NEID-DRP/>

⁶ <https://github.com/astroChasqui/q2>

⁴ <https://www.ia2.inaf.it/>

3.3. Chromospheric activity

The lower chromosphere Ca II H&K emission was measured on HARPS-N spectra using YABI (see Sect. 2.4). The average value of the S-index calibrated in the Mt. Wilson scale (Baliunas et al. 1995) is 0.45, which corresponds to $\log R'_{\text{HK}} = -4.55 \pm 0.03$. For the $\log R'_{\text{HK}}$ determination, we adopted the colour index $(B - V)_0 = 0.92$ mag, which was derived from the APASS DR10 (Henden et al. 2016) observed values.

3.4. Rotation period

The wide dataset we collected allowed us to perform a precise estimate of the stellar rotation period, which is a key parameter for age determination and star-planet system orientation. First, we inspected the ASAS-SN photometry and ran the Generalised Lomb-Scargle (GLS) periodogram algorithm (Zechmeister & Kürster 2009), which revealed the most powerful peak with a period of about 20.8 days.

We then estimated the rotation period in our fully Bayesian analysis (see Sect. 4) by leaving it free to vary and modelling the activity in our *TESS*-corrected light curves (that preserve stellar variability), RV, FWHM, and $\log R'_{\text{HK}}$ series. To support our findings, we used the GLS periodogram analysis to examine the two spectroscopic activity indicators and the RVs. All the periodograms show a dominant peak close to 20-22 days. Most *TESS* sectors also show the highest peak around 21 days, with occasional signals close to 10 or 16 days. The latter periodicities could occur, for example, if there were two similarly sized spots in opposite hemispheres.

Based on these considerations, we adopt the P_{rot} value from our full analysis (see Table 2) as the reference one, while we interpreted the 10-day signal as the first harmonic. As we detail below, this interpretation is further supported by multiple diagnostics. The expected rotation period from the $\log R'_{\text{HK}}$ value is 19.9 d using the Mamajek & Hillenbrand (2008) calibration. This further supports the adopted period as the true one.

3.5. Lithium abundance and projected rotational velocity

As an additional age estimate, we examined the possible presence of the lithium absorption line at λ 6707 Å. The line was indeed detected, and we measured an equivalent width of 1.9 ± 0.3 mÅ. Combining this value with the effective temperature derived above, and applying the EAGLES (Empirical AGes from lithium Equivalent widthS; Jeffries et al. 2023) code, we derived a lower limit of 800 Myr.

The projected rotational velocity of TOI-1533 was determined using the calibration between the FWHM of the CCF and $v \sin i_*$ developed by Rainer et al. (2023), yielding a value of $v \sin i_* = 2.5 \pm 0.5$ km s⁻¹.

4. Analysis

4.1. Joint times series Bayesian analysis

To assess the planetary properties of TOI-1533 b and TOI-1533 c, we modelled all the *TESS*-corrected light curves and ground-based ones simultaneously with the HARPS-N spectroscopic time series. We did so by using PyORBIT⁷ (Malavolta et al. 2016, 2018), a python package that models planetary transits and radial velocity signals while considering stellar activity effects. We

Table 1: Stellar properties of TOI-1533.

Parameter	TOI-1533	Reference
α (J2000)	+23:40:59.21	<i>Gaia</i> DR3
δ (J2000)	+57:29:06.87	<i>Gaia</i> DR3
μ_α (mas yr ⁻¹)	+19.78 \pm 0.01	<i>Gaia</i> DR3
μ_δ (mas yr ⁻¹)	-34.47 \pm 0.01	<i>Gaia</i> DR3
RV (km s ⁻¹)	-23.73 \pm 0.30	<i>Gaia</i> DR3
π (mas)	10.00 \pm 0.01	<i>Gaia</i> DR3
RUWE	1.1	<i>Gaia</i> DR3
V (mag)	10.98 \pm 0.04	Henden et al. (2016)
$B - V$ (mag)	0.92 \pm 0.04	Henden et al. (2016)
G (mag)	10.6843 \pm 0.0005	<i>Gaia</i> DR3
G_{BP} (mag)	11.156 \pm 0.002	<i>Gaia</i> DR3
G_{RP} (mag)	10.058 \pm 0.001	<i>Gaia</i> DR3
$G_{\text{BP}} - G_{\text{RP}}$ (mag)	1.098 \pm 0.002	<i>Gaia</i> DR3
J (mag)	9.34 \pm 0.03	2MASS
H (mag)	8.96 \pm 0.03	2MASS
K (mag)	8.83 \pm 0.02	2MASS
$T_{\text{eff,spec}}$ (K)	5146 \pm 81	This paper (Sect. 3.1)
$\log g$	4.50 \pm 0.15	This paper (Sect. 3.1)
ξ	1.09 \pm 0.20	This paper (Sect. 3.1)
[Fe/H] (dex)	+0.24 \pm 0.06	This paper (Sect. 3.1)
$\log R'_{\text{HK}}$	-4.55 \pm 0.03	This paper (Sect. 3.3)
$v \sin i_*$ (km s ⁻¹)	2.5 \pm 0.5	This paper (Sect. 3.5)
P_{rot} (d)	20.02 ^{+0.37} _{-0.33}	This paper (Sect. 4)
EW_{Li} (mÅ)	1.9 \pm 0.3	This paper (Sect. 3.5)
Luminosity (L_\odot)	0.45 \pm 0.03	This paper (Sect. 3.2)
Radius (R_\odot)	0.849 \pm 0.004	This paper (Sect. 3.2)
Mass (M_\odot)	0.88 \pm 0.04	This paper (Sect. 3.2)
Density (ρ_\odot)	1.44 \pm 0.07	This paper (Sect. 3.2)
E(B-V)	0.041 \pm 0.003	This paper (Sect. 3.2)
Age (Gyr)	6.9 ^{+1.8} _{-3.4}	This paper (Sect. 3.2)
Distance (pc)	99.7 ^{+0.4} _{-0.3}	<i>Gaia</i> DR3

tried various approaches to model the activity using Gaussian processes (GPs, Rasmussen et al. 2006; Haywood et al. 2014).

We modelled the planetary transits, the stellar activity and the Keplerian signals within the RV series, by simultaneously fitting: the time of inferior conjunction (T_0), the planetary-to-star radius ratio (R_p/R_*), the impact parameter (b), the orbital period (P_{orb}), the RV semi-amplitude (K), the stellar density (ρ_*), the quadratic limb-darkening (LD) coefficients, u_1 and u_2 , adopting the LD parameterisation introduced by Kipping (2013), the systemic RV (offset), and a jitter term added in quadrature to measurement errors for each photometric and RV datasets. This accounts for effects not modelled (e.g. short-term stellar activity) or potential underestimation of existing error bars. We fitted the orbital periods and semi-amplitudes in linear space. We assumed a circular orbit for both planets, while we imposed Gaussian priors on u_1 and u_2 . These coefficients were estimated using PyLDTk⁸ (Husser et al. 2013a; Parviainen & Aigrain 2015), taking into account the specific filters used during the observations and adding 0.1 in quadrature to their Gaussian errors to account for the known model underestimation. The complete list of priors can be found in Table 2.

We modelled stellar activity in the RV, FWHM, $\log R'_{\text{HK}}$, and *TESS* sector 84 time series using a multidimensional GP, while we used a unidimensional one for all other *TESS* photometric time series. We used an exponential-sine periodic (ESP) kernel as defined in Delisle et al. (2020, 2022) for the multidimensional GP, and a rotation kernel as defined in Foreman-Mackey et al.

⁷ <https://pyorbit.readthedocs.io/>

⁸ <https://github.com/hparvi/ldtk>

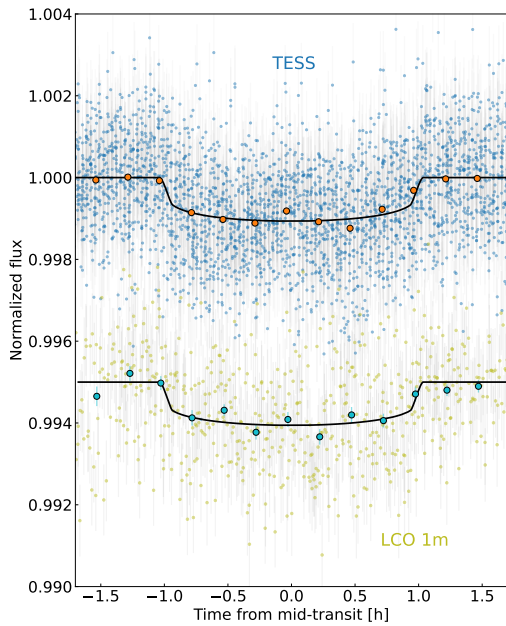


Fig. 1: Photometric modelling of TOI-1533 b planetary signal. *TESS* phase-folded transits of TOI-1533 b after normalisation together with the transit model (black line). Ground-based light curves are included as well.

(2017); Foreman-Mackey (2018) for the unidimensional ones. A unique stellar rotation period (P_{rot}) was shared between the multidimensional GP and the *celerite2* GPs. The other GP hyperparameters, such as the characteristic decay timescale (P_{dec}) and coherence scale (ω_{cs}), are independent between the photometric and spectroscopic datasets.

We first performed a global optimisation of the parameters by running PyDE (Storn & Price 1997; Parviainen 2016) for 50 000 generations and subsequently conducted a Bayesian analysis using *emcee* Foreman-Mackey et al. (2013) for 100 000 steps. We used $4 \times n_{\text{dim}}$ walkers, with n_{dim} the model dimensionality, and discarded the first 25 000 steps as burn-in. We applied a thinning factor of 100 to mitigate chain auto-correlation. Figures 1, 2, 3, F.1 and Tables 2 and F.1 show the result of the modelling.

4.2. Simultaneous photometry as part of the multidimensional GP framework

The simultaneous photometric (*TESS*) and spectroscopic (HARPS-N) observations have been fundamental to disentangle the Keplerian signals from the stellar activity. In particular, sectors 84 and 85 of *TESS* covered most of the HARPS-N observation timespan, enabling more than one stellar rotation period to be modelled simultaneously alongside the spectroscopic activity indicators. We included the simultaneous photometry as one of the observables in the multidimensional GP formalism introduced by Rajpaul et al. (2015), but did not use its first derivative. However, after careful inspection (further detailed in Appendix A) of the *TESS* photometry, we decided not to include sector 85 in the multidimensional GP. We hence performed the analysis with a four-dimensional GP model as follows:

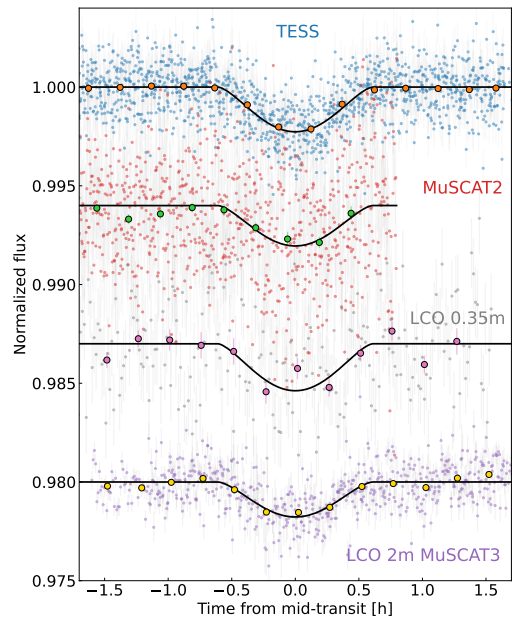


Fig. 2: Same as Figure 1 but for planet c. The *MuSCAT2* lightcurve is in the Sloan i' filter, while the *MuSCAT3* ones in the Sloan g' .

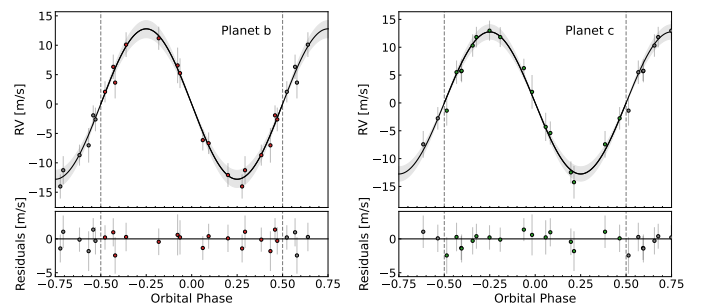


Fig. 3: Phase-folded RV curves of TOI-1533 b and c. The shaded area shows the uncertainties ($\pm 1\sigma$) of the RV model. The residuals of the fit are shown in the *bottom* panel. *Left*: Planet b. *Right*: Planet c.

$$\begin{aligned}
 \Delta RV &= V_c G(t) + V_r \dot{G}(t), \\
 \text{FWHM} &= L_c G(t), \\
 \log R'_{\text{HK}} &= L2_c G(t), \\
 \text{Flux} &= L3_c G(t),
 \end{aligned} \tag{1}$$

where $G(t)$ and $\dot{G}(t)$ are the GP and its time derivative, while $V_c, V_r, L_c, L2_c, L3_c$ coefficients characterise the amplitude of $G(t)$ and $\dot{G}(t)$ for each time series (see e.g. Barragán et al. 2022).

Table 3 compares the case in which we considered the simultaneous photometry as part of the multidimensional modelling with the case in which we did not. It is worth noting that, while the amplitudes of both planetary signals remain similar, the RV jitter is reduced by more than 50% when we consider simultaneous photometry as part of the model. When we included the photometry, the GP amplitudes of the RV datasets remain statistically consistent, but their uncertainty decreased. The uncertainty in the stellar hyperparameters and coefficients also decreased. This inclusion provided a better constraint on all the GP hyper-

Table 2: Priors and confidence intervals of the main parameters from spectroscopic plus photometric modelling.

Planetary parameters		TOI-1533 b		TOI-1533 c	
Parameter	Unit	Prior	Value	Prior	Value
Orbital period (P_{orb})	days	$\mathcal{U}(3.5, 3.7)$	3.6457974 ± 0.0000034	$\mathcal{U}(8.0, 8.1)$	8.0637926 ± 0.0000052
Central time of transit (T_0)	BTJD	$\mathcal{U}(2877.6, 2877.8)$	2877.6762 ± 0.0005	$\mathcal{U}(2853.8, 2854.0)$	2853.8872 ± 0.0005
Scaled semi-major axis ($\frac{a}{R_\star}$)		...	11.26 ± 0.17	...	19.11 ± 0.29
Orbital semi-major axis (a)	AU	...	0.0445 ± 0.0008	...	0.076 ± 0.002
Orbital inclination (i)	deg	...	86.92 ± 0.14	...	86.64 ± 0.17
Orbital eccentricity (e)		0.0	0.0	0.0	0.0
Impact parameter (b)		$\mathcal{U}(0, 2)$	0.61 ± 0.02	$\mathcal{U}(0, 2)$	1.12 ± 0.05
Planet/star radius ratio ($\frac{R_p}{R_\star}$)		$\mathcal{U}(0, 0.25)$	0.0312 ± 0.0005	$\mathcal{U}(0, 0.25)$	0.18 ± 0.05
Argument of pericenter (ω)	deg	...	90	...	90
Mean longitude (L)	deg	...	65.07 ± 0.05	...	282.30 ± 0.02
Transit duration (T_{14}) ^a	hours	...	2.07 ± 0.02	...	1.22 ± 0.02
RV semi-amplitude (K)	m s^{-1}	$\mathcal{U}(0.01, 2000)$	$12.8_{-1.5}^{+1.4}$	$\mathcal{U}(0.01, 2000)$	12.8 ± 1.3
Planetary radius (R_p)	R_\oplus	...	2.89 ± 0.06	...	$> 7.5^b$
Planetary mass (M_p)	M_\oplus	...	$28.1_{-3.4}^{+3.3}$...	$36.6_{-3.9}^{+4.0}$
Planetary density (ρ_p)	g cm^{-3}	...	6.5 ± 0.9	...	< 0.48

Stellar parameters		TOI-1533	
Parameter	Unit	Prior	Value
RV jitter	m s^{-1}	...	$1.1_{-0.8}^{+1.3}$
RV offset	m s^{-1}	...	$-23736.8_{-3.0}^{+2.6}$
Density (ρ_\star)	ρ_\odot	$\mathcal{N}(1.44, 0.07)$	1.44 ± 0.07
Rotation period (P_{rot})	days	$\mathcal{U}(10, 40)$	$20.02_{-0.33}^{+0.37}$
Decay Timescale of activity (P_{dec})	days	$\mathcal{U}(20, 1000)$	$28.1_{-5.3}^{+8.0}$
Coherence scale (ω_{cs})		$\mathcal{N}(0.350, 0.035)^c$	0.37 ± 0.03

Notes. ^(a) From Winn (2010). ^(b) 0.13th percentile lower limit. ^(c) e.g. Nardiello et al. (2022).

Table 3: Comparison of the hyperparameters of the two multidimensional GPs used to model the stellar activity.

Parameter	w/o photometry	w photometry
$\sigma_{\text{jitter}}^{\text{RV}}$ (m s^{-1})	$3.3_{-2.1}^{+2.3}$	$1.1_{-0.8}^{+1.3}$
K_b (m s^{-1})	$12.3_{-2.1}^{+2.2}$	$12.8_{-1.5}^{+1.4}$
K_c (m s^{-1})	$12.8_{-2.1}^{+2.2}$	$12.8_{-1.3}^{+1.3}$
P_{rot} (days)	$20.66_{-0.41}^{+0.62}$	$20.02_{-0.33}^{+0.37}$
P_{dec} (days)	$52.3_{-8.3}^{+20}$	$28.1_{-5.3}^{+8.0}$
V_c (m s^{-1})	$7.6_{-2.9}^{+3.6}$	$5.8_{-1.5}^{+2.1}$
V_r (m s^{-1})	$19.1_{-8.5}^{+9.7}$	$18.3_{-4.3}^{+5.8}$
L_c (km s^{-1})	$0.04_{-0.01}^{+0.02}$	0.03 ± 0.01
L_{2c}	$0.04_{-0.01}^{+0.02}$	0.03 ± 0.01

Notes. We omitted the coherence scale (ω_{cs}) as its value is mainly driven by the prior.

parameters, which in turn reduced the RV jitter. We therefore adopted the latter model as the reference one (see Figure 4).

Lastly, we want to emphasise that we repeated the analysis, allowing the eccentricity to vary. However, our analysis showed a clear preference for case 1 (circular) over case 2 (eccentric), with a significant ΔBIC_{21} value of 64 (Kass & Raftery 1995). Even when only the eccentricity of the inner planet is allowed to vary (case 3), case 1 is favoured, with a significant ΔBIC_{31} of 20. The same is true when the eccentricity of the outer planet is allowed to vary (case 4), with a significant ΔBIC_{41} of 18.

4.3. Joint modelling with NEID data

We included the NEID RVs in the simultaneous photometric and spectroscopic analysis using PyORBIT, but there was no improvement compared to using only the HARPS-N and TESS data. While the NEID RVs do agree with the stellar activity model, the uncertainty in the activity coefficients is greater most likely because the seven NEID data points are too sparse and widely separated in time from the HARPS-N RVs. This made it difficult to properly model the stellar activity contribution in the NEID data.

Nevertheless, the NEID data are an important addition to the analysis presented in the previous Section. In particular, the peak-to-peak RV variation is comparable in both datasets (see Figs. F.1 and F.6), which confirms the significance of the activity contribution and the two Keplerian signal amplitudes. Moreover, this result highlights that the Gaussian Process we used is robust and did not overfit the data, given the difficulty in modelling the two widely separated datasets.

4.4. Search for transit timing variations

We explored the possible presence of dynamical interactions in the system by performing a search for transit timing variations (TTVs, e.g. Agol et al. 2005; Holman & Murray 2005) of both planets, using a PyORBIT model based on the BATMAN code. We fitted each transit time, T_0 , fixing the orbital periods described in Sect. 4.

We prepared the observed (O) minus calculated (C) diagrams by removing the linear ephemeris for each T_0 . The O–C diagrams are presented in Figs. F.2 and F.3. Interestingly, for the inner planet TOI-1533 b, the possible TTV amplitude (A_{TTV}), computed as the semi-amplitude of the O–C, is 24 ± 7

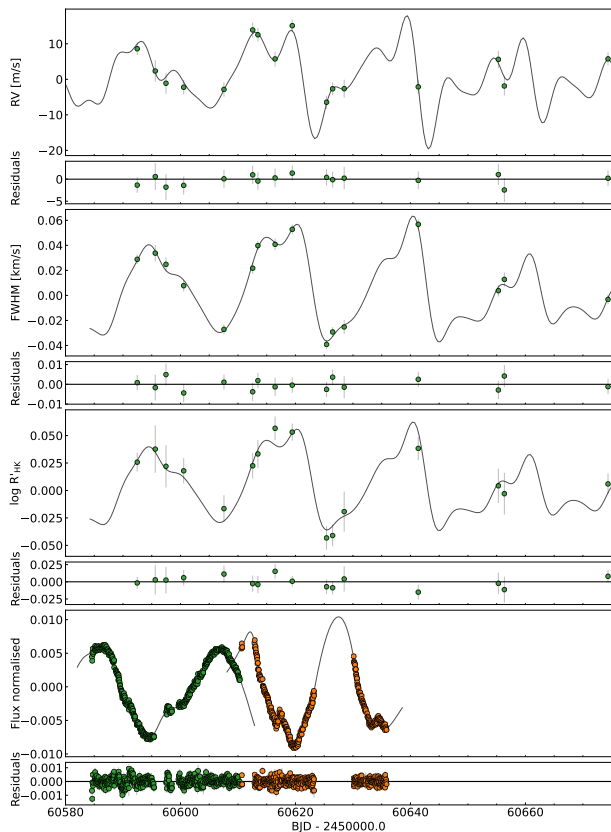


Fig. 4: Multi-dimensional GP model of stellar activity in the RV, FWHM, $\log R'_{\text{HK}}$, and photometric time series. Each panel shows the time series modelling and the respective residuals of the fit. *Top panel:* RV time series without Keplerian signals. *Bottom:* Photometric time series of simultaneous *TESS* sectors 84 and 85. Sector 85 is shown in a different colour because it has not been included in the multidimensional GP framework; instead, it has been modelled with a unidimensional GP (see Appendix A for further clarification).

minutes (with the uncertainty estimated as in Mantovan et al. 2024b). The reduced χ^2 value of the linear ephemeris is about 7, which suggests the hypothesis of ongoing dynamical interaction between planets b and c – likewise recently suggested by Nabbie et al. (2026).

Motivated by this finding, we performed a dynamical analysis using the N -body dynamical integrator TRADES⁹ (Borsato et al. 2014, 2019, 2021). While our analysis (see Appendix B) successfully retrieved planetary parameters consistent with those reported in Table 2, our dynamical model is not capable of reproducing the observed transit times with a total reduced χ^2 of 7 for the best-fit configuration. The residuals could be the results of low-accuracy and low-precision observations, additional body/ies in the system, or in-transit stellar activity in the form of stellar spots affects the *TESS* data. Only exquisite, high-precision photometry, such as that provided by CHEOPS (Benz et al. 2021), could determine if the observed variation is of planetary or stellar origin.

4.5. Planet equilibrium temperature and TSM

We estimated the equilibrium temperature of both planets assuming zero albedo and full day-night heat redistribution with the simple equation $T_{\text{eq}} = T_{\text{eff}} \sqrt{\frac{R_{\star}}{a}} \left(\frac{1}{4}\right)^{1/4}$ with T_{eff} the stellar effective temperature, R_{\star} the stellar radius, and a the orbital semi-major axis. We found $T_{\text{eq}} = 1084 \pm 20$ K for TOI-1533 b and $T_{\text{eq}} = 829 \pm 17$ K for planet c.

Therefore, we derived the transmission spectroscopy metric (TSM, Kempton et al. 2018) for planet b to be 20 ± 3 by inserting the estimated equilibrium temperature into the TSM equation. In contrast, due to the grazing nature of TOI-1533 c (see Table 2), we were unable to obtain a precise TSM estimation for the outer companion. Nevertheless, based on the minimum retrieved radius, we could set a minimum TSM value of about 200. However, to compensate for the fact that the signal-to-noise ratio of an atmospheric observation scales as the square root of the transit duration, we adjusted the TSM to account for the grazing nature of TOI-1533 c. We estimated the scaling factor as $\sqrt{T_{14, b>1}/T_{14, b=0}} = \sqrt{1.22/3.8} = 0.566$, where $T_{14, b=0} \approx \frac{P R_{\star}}{\pi a}$ from Nascimbeni et al. (2026), implying a corrected $\text{TSM}_{\text{corr}} \approx 110$. Therefore, even with this correction, the minimum TSM value would imply that TOI-1533 c is a high-quality atmospheric characterisation target.

4.6. Ephemeris improvements and future observations

Propagating the new ephemeris to 1 January 2030 reduces the level of uncertainty for TOI-1533 b to 4.2 minutes and for TOI-1533 c to 3.4 minutes. At present, no further *TESS* observations are planned for this target.

5. Discussion

5.1. A new compact multi-planet system with a hot gas giant

This paper confirms TOI-1533 as one of only a handful of multi-planet systems with a short-period giant planet and an inner, small-size planet companion. Such multi-planets systems are a new and emerging category of planetary systems architecture (see e.g. Howe et al. 2025) that can help us to better understand formation and migration mechanisms. They also play a key role in linking the exoplanet population to the architecture and dynamics of the Solar System.

TOI-1533 b is a transiting sub-Neptune with a radius of $R_p = 2.89 \pm 0.06 R_{\oplus}$ and a mass of $M_p = 28.1^{+3.3}_{-3.4} M_{\oplus}$, which orbits a K dwarf star in about 3.6 days. Its outer companion, TOI-1533 c, is instead a grazing giant planet with a minimum radius of $7.5 R_{\oplus}$ (0.13th percentile lower limit, see also Fig. F.11) and a mass of $M_p = 36.6^{+4.0}_{-3.9} M_{\oplus}$, about 1/3 that of Saturn. From the minimum radius, we can derive a maximum planetary density of $\rho_p < 0.48 \text{ g cm}^{-3}$, which is compatible with a hot gas giant planet primarily composed of H/He by volume and mass (e.g. Lopez & Fortney 2014; Zeng et al. 2019). Compared to small-size planets orbiting interior to short-period giant planets (see Fig. 5), TOI-1533 b is instead the most massive, with a mass almost double that of Neptune and about 75% of its outer giant companion. Moreover, TOI-1533 b joins a rare subpopulation of Neptunian planets with high densities (see Osborn et al. 2023; Armstrong et al. 2020; Naponiello et al. 2023). Notably, it is the only one of these planets known to be in a multi-planet system.

⁹ <https://github.com/lucaborsato/trades>

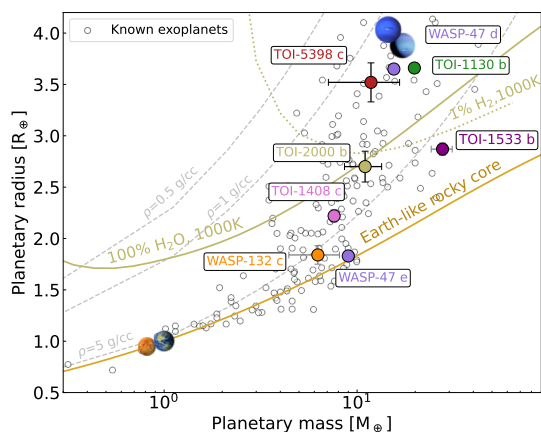


Fig. 5: Mass–radius diagram of all confirmed small planets ($R_p < 4R_\oplus$) with mass and radius precisions better than 20% (Christiansen et al. 2025). The masses of the plotted, small inner companions of hot giants have been taken from references listed in Tab. E.1. We included theoretical mass–radius curves for various planetary pure compositions from Zeng et al. (2019). Grey dashed curves show densities $\rho = 0.5, 1,$ and 5 g cm^{-3} .

5.2. Architecture of systems hosting hot, intermediate-mass planets

It is their mass ratio, together with the low mass of the large-size outer companion, that makes this system quite unusual compared to classical HJs with inner low-mass companions. Motivated by these findings, we selected all the confirmed planets (Christiansen et al. 2025) similar to TOI-1533 c, and that have inner companions of any kind. Our selection criteria – for the outer planet – were the following:

- Orbital period shorter than 20 days;
- Planetary radius $R_p > 4 R_\oplus$;
- Planetary mass M_p between $15 M_\oplus$ and $120 M_\oplus$, to include Neptunes and Saturns.

We found a total of eleven systems (Fig. 6, Tab. E.1). One interesting trend emerging is the preponderance of metal-rich stars, with the only two stars with solar metallicity (Kepler-25, K2-32) hosting the two least massive planets (about $15 M_\oplus$ each). This common characteristic becomes even more intriguing if we include the other six compact systems with short-period giants (see Tab. E.1), as they also orbit metal-rich stars. This result follows the well-known trend that planets are more frequent around metal-rich stars (Santos et al. 2001, 2004). It is particularly evident for giant planets, as the likelihood of their formation increases around such stars, as predicted by the core-accretion model (Mordasini et al. 2008). However, it is rather peculiar that none of the selected systems is hosted by a metal-poor star. By contrast, about 20% of single-planet systems with these characteristics orbit metal-poor stars.

Figure 6 seems to also suggest that stars with larger radii and masses (F-G dwarfs) tend to have hot Saturn planets in terms of masses, while smaller stars (K dwarfs) seem to host less massive planets, such as hot Neptunes and super-Neptunes (see Fig. 7). Also in this case, Kepler-25 appears unusual as it is an F-type star hosting the lowest-mass outer planet in the sample. However, the system also hosts a 120-day Saturn-mass planet. In Fig. 7, we highlighted pairs of planets with similar masses, including TOI-1533. Interestingly, the sizes, masses, and periods of the planets orbiting Kepler-411 are comparable to those of TOI-1533, with

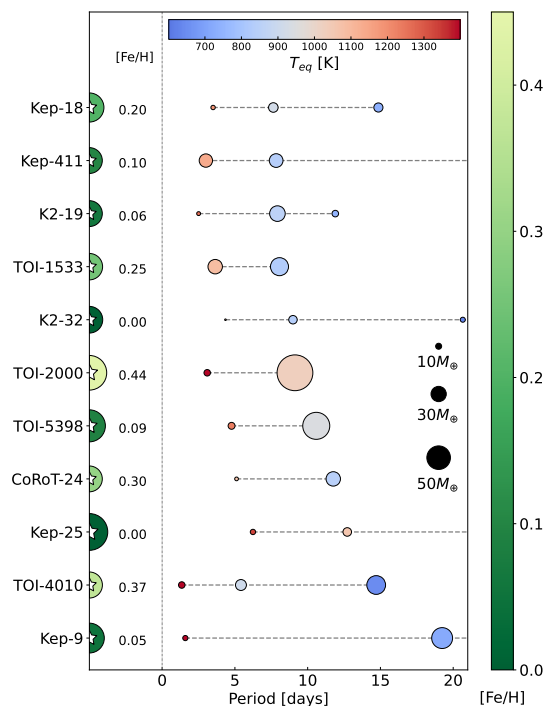


Fig. 6: Architecture of multi-planet systems hosting an intermediate-mass planet ($15M_\oplus < M_p < 120M_\oplus$, $R_p > 4R_\oplus$) and an inner companion, both in close-in orbits ($P < 20 \text{ d}$). Each row represents a planetary system (vertical axis) and the planetary orbital periods (horizontal axis). The systems are sorted in ascending order of the period of the intermediate-mass planet. The equilibrium temperature of the planets is colour-coded (top colour bar), while the dot size tracks planetary masses. The host stars are indicated by semi-circular dots, colour-coded by stellar metallicity (right colour bar) and with sizes that encode their radii. Dashed lines indicate outermost planets not shown.

the inner planet being primarily rocky and the outer one having gases dominating its volume. However, Kepler-411 also has two known planets at longer orbital periods. We explore this further in Sect. 5.5.

5.3. Migration history implications

In light of their possible shared disc-driven migration history, we inspected whether the selected multi-planet systems exhibit similar characteristics. As shown in simulations by Raymond et al. (2006), at early stages of planetary formation, systems with a planet orbiting interior to a close-in giant often cluster near mean-motion resonances (i.e. where the period ratio $\mathcal{P} \equiv P_2/P_1$ can be expressed as a rational number i/j), where gravitational interactions can lead to detectable TTVs. However, the resonant configuration can be disrupted by disc dissipation (e.g. Turrini et al. 2023) or diverging planet evolution at late times. The latter is likely to result from either mass loss due to photoevaporation, or from different tidal interaction strengths with the star, causing the inner companion to detach and increase \mathcal{P} . In Fig. 8, we show the orbital period of the inner planets (P_1) as a function of the planet pair period ratio (\mathcal{P}). There is a clear upward trend in the values of \mathcal{P} towards shorter orbital periods, with the largest period ratios observed for planets within two days (TOI-4010 b and Kepler-9 d, the latter being even outside the y-axis range), in line with a very recent finding by

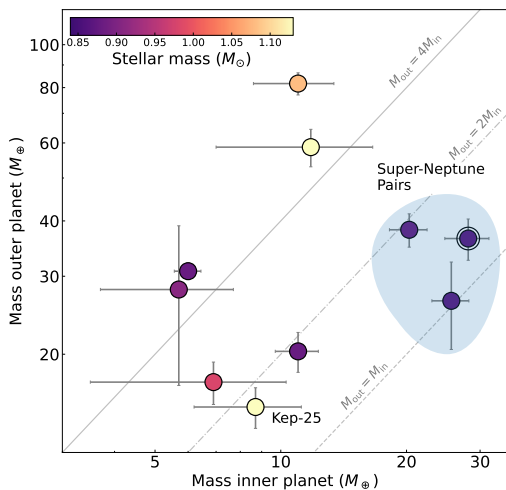


Fig. 7: Inner planet mass vs. outer planet mass for all the systems in Fig. 8. The stellar mass is colour-coded, while the blue area highlights planet pairs with similar masses. TOI-1533 is indicated by two black circles.

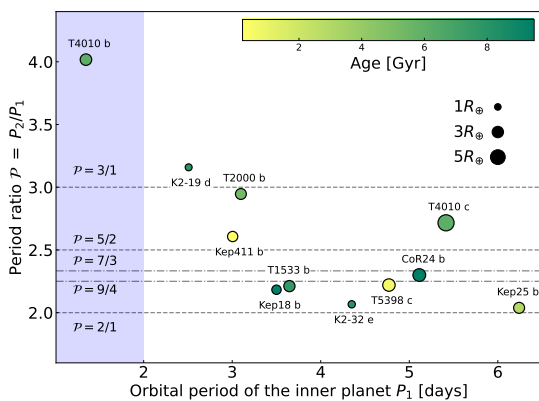


Fig. 8: Orbital period P_1 as a function of the period ratio $\mathcal{P} = P_2/P_1$ for all planets interior to close-in intermediate-mass planets ($15M_{\oplus} < M_p < 120M_{\oplus}$, $R_p > 4R_{\oplus}$). The age of the system is colour-coded, and the dot size tracks the radius of the planet it represents. Horizontal lines represent some low-order mean-motion resonances, and the blue area highlights planets with orbits shorter than two days.

Goyal & Wang (2025). It is worth noting that planets with larger \mathcal{P} , but similar P_1 , tend to have larger R_p values.

Planets undergoing disc-driven migration may share two common characteristics that influence their natural photoevaporation resistance. First, they arrive in close-in orbits in a short time – $\lesssim 10$ Myr – exposing them to the full, constant XUV irradiation during the stellar active phase. This contrasts with planets undergoing late HEM, which can arrive close-in much later and may have escaped this active phase (Bourrier et al. 2018; Attia et al. 2021). Another possible driver of atmospheric erosion is the lower atmospheric metallicity and C/O ratios foreseen for planets undergoing disc-migration (Madhusudhan et al. 2014; Penzlin et al. 2024; Claringbold et al. 2026). This may in turn make these planets less resistant to photoevaporation, resulting in greater mass loss (e.g. Wilson et al. 2022; Mantovan et al. 2024b). Motivated by these two characteristics, we compared Neptune-mass planets with inner companions to those in single-planet systems (or whose companions are outer, long-period

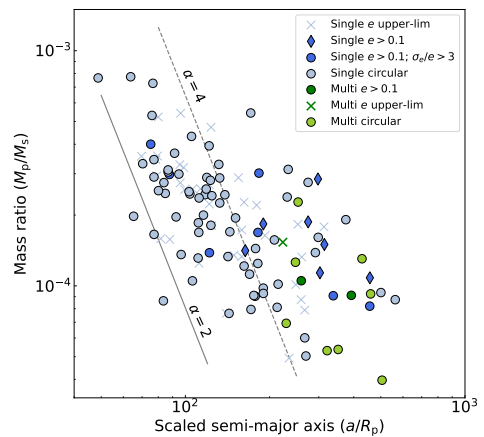


Fig. 9: Tidal diagram of intermediate-mass planets in single- and close-in multi-planet systems. Single-planet systems are coloured light-blue (circular) and blue (eccentric), with different shapes based on their eccentricity precision. Multi-planet systems are coloured green (eccentric) and light-green (circular). The solid and dashed lines stand for $a = 2a_R$ and $a = 4a_R$, with a_R the Roche limit.

ones). To this end, we generated a tidal diagram of scaled semi-major axis (a/R_p) versus mass ratio (M_p/M_s) for all Neptune-mass planets in single and multi-planet systems (Fig. 9), distinguishing between circular and eccentric orbits.

Planets in close-in multis tend to have larger scaled semi-major axes – which is possibly due to the inner companion hindering the inward migration of the outer planet – and potentially lower masses. This possible trend may indicate greater atmospheric erosion for planets undergoing disc-driven migration. It is also worth noting that almost all planets with $\alpha < 4$ are on circular orbits, as would be expected given that the timescale for tidal circularisation increases with increasing α values (Goldreich & Soter 1966; Bonomo et al. 2017).

5.4. Prospects for atmospheric follow-up

The unusual architecture of this system provides a valuable laboratory for investigating the interplay between planet formation and atmospheric composition. The atmospheres of its planets are expected to preserve chemical fingerprints of their accretion histories, encoding information about where and how material was accreted within the protoplanetary disk (Öberg et al. 2011). Since disk chemistry varies with radial distance, particularly across major ice lines, different solid-to-gas accretion ratios imprint distinct elemental and molecular signatures on planetary atmospheres. In particular, the relative abundances of water- and carbon-bearing species, as well as the ratio of volatiles to refractories, may provide key constraints on formation location and migration history (Lothringer et al. 2021; Pacetti et al. 2022; Chachan et al. 2023).

In this system, the orbital architecture will strongly influence the atmospheric properties of the smaller inner planet. The presence of an outer gas giant companion is expected to regulate or inhibit the inward drift of icy pebbles (Easterwood et al. 2024), thereby altering the volatile budget of the inner disk where TOI-1533 b formed. Such a mechanism would directly affect the planet’s water enrichment and, consequently, observable abundance ratios such as the carbon-to-oxygen ratio (C/O), potentially favouring a higher C/O ratio.

The most observationally accessible planet in the system is TOI-1533 c ($TSM \geq 200$ and $TSM_{\text{corr}} \approx 110$, compared to $TSM \approx 20$ for TOI-1533 b). Despite its grazing nature, this high TSM places the outer giant among the most favourable targets for atmospheric characterisation at its equilibrium temperature (Fig. F.9, where we did not use the corrected TSM value to ensure consistency with all literature values). Notably, its equilibrium temperature lies near the CH_4/CO chemical transition regime, making it particularly compelling for probing carbon chemistry (Fortney et al. 2020). Infrared observations with the James Webb Space Telescope (JWST) or ground-based facilities such as IGRINS-2 would be particularly powerful for constraining the relative abundances of methane and carbon monoxide, key tracers of the atmospheric C/O ratio and disequilibrium processes (Fig. F.10). At these temperatures, vertical mixing is expected to drive significant departures from equilibrium chemistry (Visscher & Moses 2011). This is the most evident in methane, a species highly sensitive to quenching, as its abundance depends strongly on pressure and temperature. Simultaneous constraints on CH_4 and CO would therefore provide valuable insight into the planet’s internal energy budget and vertical mixing efficiency. Further prospects are detailed in Appendix D.

5.5. Search for outer companions

Besides confirming TOI-1533 b and c, we also investigated the compatibility of the data with the presence of an additional planet in the system using a posterior-based mass–period detection map (Fig. 10). To generate this map, we repeated the analysis described in Sect. 4, including an additional Keplerian component with respect to our reference model to represent a hypothetical undetected signal in the data. Wide, uninformative priors were adopted for its orbital period P_{orb} and the radial-velocity semi-amplitude K . The posterior samples obtained for this additional component were then used to explore the region of the parameter space compatible with the residuals of the adopted two-planet model. Unlike classical injection-recovery experiments, this approach directly exploits the posterior distributions, naturally preserving only physically allowed solutions.

We then computed a two-dimensional histogram of the posterior samples in the mass–period plane using 50 bins for each parameter over the range $[10\text{--}1000\text{ d}, 1M_{\oplus}\text{--}13M_J]$, and normalised the distribution within each period bin to obtain the conditional posterior density $P(M_p|P_{\text{orb}})$.

Figure 10 shows that short-period signals ($P \lesssim 200\text{ d}$) are strongly disfavoured across the entire mass range, with relative probability densities typically below 10^{-4} per period bin. The only exceptions consist of a small number of sparse solutions in the sub-giant planet regime ($M_p \lesssim 1M_J$), which likely correspond to degenerate eccentric configurations producing quasi-flat signals over the observed RV time series.

Overall, this result supports our two-planet model, including the GP treatment of stellar activity, as a robust description of the RV variability on these orbital timescales. However, as shown by the inset comparing the known outer planets of Kepler-411, the presence of additional planets in this regime around TOI-1533 cannot be definitively excluded.

At longer orbital periods, the ability of the current dataset to exclude additional companions progressively decreases: above 200 days, only massive companions with masses of a few to several Jupiter masses can be confidently ruled out, while at even longer periods, such companions remain compatible with the observations. This behaviour reflects the limited temporal baseline of the available RV data. Additional long-term RV monitoring

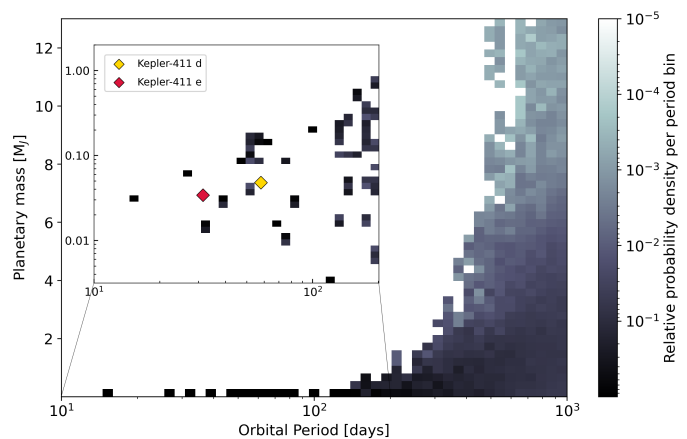


Fig. 10: Posterior-based mass–period detection map for a hypothetical additional planet in the TOI-1533 system. Darker regions indicate mass–period combinations that are compatible with the residuals of the two-planet model, while brighter regions are strongly disfavoured. The short-period regime ($P \lesssim 200$ days) is shown in detail in the logarithmic-scale inset, where the known outer planets of Kepler-411 are superimposed for comparison.

and *Gaia* DR4 astrometry will be essential to further constrain the outer system architecture and to search for potential long-period companions.

6. Conclusions

In this work, we present the discovery of TOI-1533, a multi-planet system composed of a super-Neptune-mass pair with disparate radii, orbiting an active K-dwarf star. Through the joint modelling of stellar and planetary signals from HARPS-N RVs and TESS transits, we were able to measure the planetary masses and isolate the stellar modulation. We highlight a few notable findings that emerged from this study:

- TOI-1533 is confirmed as the ninth multi-planet system comprising a close-in gas giant planet ($R_p > 7.5R_{\oplus}$, $P \approx 8.06\text{ d}$, $\rho_p < 0.48\text{ g cm}^{-3}$) and an inner, small-size companion ($R_p = 2.89 \pm 0.06R_{\oplus}$, $P \approx 3.65\text{ d}$). Despite their disparate radii, they have a large mass ratio ($M_b/M_c \approx 0.8$) and the gas giant has a low mass ($M_c \approx 40M_{\oplus}$), making this system quite unusual compared to classical HJs with inner low-mass companions;
- Jointly modelling HARPS-N RVs and *TESS* photometry using a multi-GP framework was fundamental to disentangle stellar activity from planetary signals. The inclusion of *TESS* Sector 84 in the GP formalism allowed us to halve the jitter;
- We detected possible TTVs for planet TOI-1533 b, with a reduced $\chi^2 \approx 7$, which suggests ongoing dynamical interactions. However, significant scatter in the O-C diagram residuals – likely due to in-transit stellar activity in the form of stellar spots – needs to be modelled out using future, higher-precision photometry, such as that provided by CHEOPS;
- We found a total of eleven systems hosting hot Neptunes and Saturns ($15M_{\oplus} < M_p < 120M_{\oplus}$, $P < 20\text{ d}$) with inner companions of any kind. None of these is hosted by metal-poor stars, and those orbiting F-G dwarf stars tend to be more massive than those orbiting K dwarfs;

- Small interior planets in systems with a close-in giant orbit near mean-motion resonances, with gravitational interactions leading to detectable TTVs. The resonant configuration may be disrupted by mass loss or different tidal interaction with the host star, causing the inner companion to detach and increasing the planet-pair period ratio (\mathcal{P}). We inspected the eleven systems mentioned above, and found a possible correlation between \mathcal{P} and the inner planet period (P_1), which supports recent findings by Goyal & Wang (2025).

Acknowledgements. We acknowledge the use of public TESS data from pipelines at the TESS Science Office and at the TESS Science Processing Operations Center. Funding for the TESS mission is provided by NASA’s Science Mission Directorate. This research has made use of the Exoplanet Follow-up Observation Program (ExoFOP; DOI: 10.26134/ExoFOP5) website and the NASA Exoplanet Archive, both of which are operated by the California Institute of Technology under contract with the National Aeronautics and Space Administration under the Exoplanet Exploration Program. S.W.Y. gratefully acknowledges support from the Heising-Simons Foundation. This paper contains data taken with the NEID instrument, which was funded by the NASA-NSF Exoplanet Observational Research (NN-EXPLORE) partnership and built by Pennsylvania State University. Data presented herein were obtained at the WIYN Observatory from telescope time allocated to NN-EXPLORE (2025A-381524, 2025B-123953, PI: Yee) through the scientific partnership of the National Aeronautics and Space Administration, the National Science Foundation, and NOIRLab. The authors are honored to be permitted to conduct astronomical research on Iolkam Du’ag (Kitt Peak), a mountain with particular significance to the Tohono O’odham. This work makes use of observations from the LCOGT network. Part of the LCOGT telescope time was granted by NOIRLab through the Mid-Scale Innovations Program (MSIP). MSIP is funded by NSF. This paper is based on observations made with the Las Cumbres Observatory’s education network telescopes that were upgraded through generous support from the Gordon and Betty Moore Foundation. KAC acknowledges support from the TESS mission via subaward s3449 from MIT and NASA grants 80NSSC24K1889 and 80NSSC26K0081. This paper is based on observations made with the MuSCAT3 instrument, developed by the Astrobiology Center and under financial supports by JSPS KAKENHI (JP18H05439) and JST PRESTO (JPMJPR1775), at Faulkes Telescope North on Maui, HI, operated by the Las Cumbres Observatory. This article is based on observations made with the MuSCAT2 instrument, developed by ABC, at Telescopio Carlos Sánchez operated on the island of Tenerife by the IAC in the Spanish Observatorio del Teide. This work is partly supported by JSPS KAKENHI Grant Numbers JP24H00017, JP24K17083, JP24K00689, JP21K13955, JP24K17082, JP24H00248, JP25K24620, JP26H01402, JP26K00755, and JSPS Grant-in-Aid for JSPS Fellows Grant Number JP24KJ0241. We acknowledge financial support from the Agencia Estatal de Investigación of the Ministerio de Ciencia e Innovación MCIN/AEI/10.13039/501100011033 and the ERDF “A way of making Europe” through projects PID2021-125627OB-C32 and PID2024-158486OB-C32. JK acknowledges support from the Swedish Research Council (Starting Grant 2017-04945 and Project Grant 2022-04043) and from the Spanish Research Agency of the Ministry of Science, Innovation and Universities (AEI-MICIU) under grant ‘Contribution of the IAC to the PLATO Space Mission’ with reference PID2023-149439NB-C41. F. M. acknowledges the financial support from the Agencia Estatal de Investigación del Ministerio de Ciencia, Innovación y Universidades (MCIU/AEI) through grant PID2023-152906NA-I00. LBo, VNa, GPI, PLe acknowledge the funding support from Italian Space Agency (ASI) regulated by ‘Accordo ASI-INAF n. 2013-016-R.0 del 9 luglio 2013 e integrazione del 9 luglio 2015 CHEOPS Fasi A/B/C’. We acknowledge the Italian center for Astronomical Archives (IA2, <https://www.ia2.inaf.it>), part of the Italian National Institute for Astrophysics (INAF), for providing technical assistance, services and supporting activities of the GAPS collaboration. JLL was supported by NASA’s Exoplanets Research Program grant 24-XRP24_2-0020.

References

- Agol, E., Steffen, J., Sari, R., & Clarkson, W. 2005, *MNRAS*, 359, 567
 Almenara, J. M., Mardling, R., Leleu, A., et al. 2025, *A&A*, 703, A167
 Alonso, R., Moutou, C., Endl, M., et al. 2014, *A&A*, 567, A112
 Armstrong, D. J., Lopez, T. A., Adibekyan, V., et al. 2020, *Nature*, 583, 39
 Attia, M., Bourrier, V., Eggenberger, P., et al. 2021, *A&A*, 647, A40
 Baliunas, S. L., Donahue, R. A., Soon, W. H., et al. 1995, *ApJ*, 438, 269
 Baranne, A., Queloz, D., Mayor, M., et al. 1996, *A&AS*, 119, 373
 Barragán, O., Aigrain, S., Rajpaul, V. M., & Zicher, N. 2022, *MNRAS*, 509, 866
 Barros, S. C. C., Almenara, J. M., Demangeon, O., et al. 2015, *MNRAS*, 454, 4267
 Basilicata, M., Giacobbe, P., Brogi, M., et al. 2025, *A&A*, 695, A107
 Becker, J. C., Vanderburg, A., Adams, F. C., et al. 2015, *ApJ*, 812, L18
 Benz, W., Broeg, C., Fortier, A., et al. 2021, *Experimental Astronomy*, 51, 109
 Biazzo, K., D’Orazi, V., Desidera, S., et al. 2022, *A&A*, 664, A161
 Blackwell, D. E. & Shallis, M. J. 1977, *MNRAS*, 180, 177
 Bonfanti, A., Gandolfi, D., Leonardi, P., et al. 2026, arXiv e-prints, arXiv:2604.15035
 Bonfanti, A. & Gillon, M. 2020, *A&A*, 635, A6
 Bonomo, A. S., Desidera, S., Benatti, S., et al. 2017, *A&A*, 602, A107
 Borsato, L., Degen, D., Leleu, A., et al. 2024, *A&A*, 689, A52
 Borsato, L., Malavolta, L., Piatto, G., et al. 2019, *MNRAS*, 484, 3233
 Borsato, L., Marzari, F., Nascimbeni, V., et al. 2014, *A&A*, 571, A38
 Borsato, L., Piatto, G., Gandolfi, D., et al. 2021, *MNRAS*, 506, 3810
 Bourrier, V., Lovis, C., Beust, H., et al. 2018, *Nature*, 553, 477
 Brown, T. M., Baliber, N., Bianco, F. B., et al. 2013, *PASP*, 125, 1031
 Cañas, C. I., Wang, S., Mahadevan, S., et al. 2019, *ApJ*, 870, L17
 Casagrande, L., Lin, J., Rains, A. D., et al. 2021, *MNRAS*, 507, 2684
 Castelli, F. & Kurucz, R. L. 2003, in *Modelling of Stellar Atmospheres*, ed. N. Piskunov, W. W. Weiss, & D. F. Gray, Vol. 210, A20
 Chachan, Y., Knutson, H. A., Lothringer, J., & Blake, G. A. 2023, *ApJ*, 943, 112
 Christiansen, J. L., McElroy, D. L., Harbut, M., et al. 2025, *PSJ*, 6, 186
 Claringbold, A. B., Fisher, C. E., Kirk, J., et al. 2026, *MNRAS*, 546, 143
 Cochran, W. D., Fabrycky, D. C., Torres, G., et al. 2011, *ApJS*, 197, 7
 Collier Cameron, A., Mortier, A., Phillips, D., et al. 2019, *MNRAS*, 487, 1082
 Collins, K. 2019, in *American Astronomical Society Meeting Abstracts*, Vol. 233, American Astronomical Society Meeting Abstracts #233, 140.05
 Collins, K. A., Kielkopf, J. F., Stassun, K. G., et al. 2017, *AJ*, 153, 77
 Cosentino, R., Lovis, C., Pepe, F., et al. 2012, in *SPIE*, Vol. 8446, *Ground-based and Airborne Instrumentation for Astronomy IV*, ed. I. S. McLean, S. K. Ramsay, & H. Takami, 84461V
 Covino, E., Esposito, M., Barbieri, M., et al. 2013, *A&A*, 554, A28
 Cutri, R. M., Skrutskie, M. F., van Dyk, S., et al. 2003, *2MASS All Sky Catalog of point sources*.
 Dai, F., Winn, J. N., Albrecht, S., et al. 2016, *ApJ*, 823, 115
 Dawson, R. I. & Johnson, J. A. 2018, *ARA&A*, 56, 175
 Delisle, J. B., Hara, N., & Ségransan, D. 2020, *A&A*, 638, A95
 Delisle, J. B., Unger, N., Hara, N. C., & Ségransan, D. 2022, *A&A*, 659, A182
 Dumusque, X., Cretignier, M., Sosnowska, D., et al. 2021, *A&A*, 648, A103
 Dutra-Ferreira, L., Pasquini, L., Smiljanic, R., et al. 2016, *A&A*, 585, A75
 Easterwood, W., Kalyaan, A., & Bazanti, A. 2024, *ApJ*, 977, 21
 Eggleton, P. P. & Kiseleva-Eggleton, L. 2001, *ApJ*, 562, 1012
 Espinoza, N., Steinrueck, M. E., Kirk, J., et al. 2024, *Nature*, 632, 1017
 Foreman-Mackey, D. 2018, *RNAAS*, 2, 31
 Foreman-Mackey, D., Agol, E., Ambikasaran, S., et al. 2017, *AJ*, 154, 220
 Foreman-Mackey, D., Hogg, D. W., Lang, D., et al. 2013, *PASP*, 125, 306
 Fortney, J. J., Visscher, C., Marley, M. S., et al. 2020, *AJ*, 160, 288
 Gaia Collaboration, Vallenari, A., Brown, A. G. A., et al. 2023, *A&A*, 674, A1
 Gavel, D., Kupke, R., Dillon, D., et al. 2014, in *SPIE*, Vol. 9148, *Adaptive Optics Systems IV*, ed. E. Marchetti, L. M. Close, & J.-P. Vran, 914805
 Goldreich, P. & Soter, S. 1966, *Icarus*, 5, 375
 Goyal, A. V. & Wang, S. 2025, *AJ*, 169, 191
 Grieves, N., Bouchy, F., Armstrong, D. J., et al. 2025, *A&A*, 693, A144
 Guillot, T. 2010, *A&A*, 520, A27
 Halverson, S., Terrien, R., Mahadevan, S., et al. 2016, in *Ground-Based and Airborne Instrumentation for Astronomy VI*, Vol. 9908 (SPIE), 2022–2041
 Haywood, R. D., Collier Cameron, A., Queloz, D., et al. 2014, *MNRAS*, 443, 2517
 Henden, A. A., Templeton, M., Terrell, D., et al. 2016, *VizieR Online Data Catalog: AAVSO Photometric All Sky Survey (APASS) DR9 (Henden+, 2016)*, *VizieR On-line Data Catalog: II/336*. Originally published in: 2015AAS...22533616H
 Holman, M. J., Fabrycky, D. C., Ragozzine, D., et al. 2010, *Science*, 330, 51
 Holman, M. J. & Murray, N. W. 2005, *Science*, 307, 1288
 Hord, B. J., Colón, K. D., Berger, T. A., et al. 2022, *AJ*, 164, 13
 Howard, A. W., Johnson, J. A., Marcy, G. W., et al. 2010, *ApJ*, 721, 1467
 Howe, A. R., Becker, J. C., Stark, C. C., & Adams, F. C. 2025, *AJ*, 169, 149
 Howell, S. B., Everett, M. E., Sherry, W., Horch, E., et al. 2011, *AJ*, 142, 19
 Huang, C. X., Quinn, S. N., Vanderburg, A., et al. 2020, *ApJ*, 892, L7
 Hunter, A., Macgregor, A., Szabo, T., Wellington, C., & Bellgard, M. 2012, *Source Code for Biology and Medicine*, 7
 Husser, T. O., Wende-von Berg, S., Dreizler, S., et al. 2013a, *A&A*, 553, A6
 Husser, T. O., Wende-von Berg, S., Dreizler, S., et al. 2013b, *A&A*, 553, A6
 Isaacson, H., Howard, A. W., Fulton, B., et al. 2024, *ApJS*, 274, 35
 Jeffries, R. D., Jackson, R. J., Wright, N. J., et al. 2023, *MNRAS*, 523, 802
 Jensen, E. 2013, *Tapir: A web interface for transit/eclipse observability*, *Astrophysics Source Code Library*
 Kass, R. E. & Raftery, A. E. 1995, *Journal of the American Statistical Association*, 90, 773
 Kempton, E. M. R., Bean, J. L., Louie, D. R., et al. 2018, *PASP*, 130, 114401
 Kipping, D. M. 2013, *MNRAS*, 435, 2152
 Kochanek, C. S., Shappee, B. J., Stanek, K. Z., et al. 2017, *PASP*, 129, 104502

- Komacek, T. D. & Showman, A. P. 2016, *ApJ*, 821, 16
- Korth, J., Chaturvedi, P., Parviainen, H., et al. 2024, *ApJ*, 971, L28
- Kunimoto, M., Vanderburg, A., Huang, C. X., et al. 2023, *AJ*, 166, 7
- Kupke, R., Gavel, D., Roskosi, C., et al. 2012, in *SPIE*, Vol. 8447, Adaptive Optics Systems III, ed. B. L. Ellerbroek, E. Marchetti, & J.-P. Véran, 84473G
- Leonardi, P., Borsato, L., Pagliaro, L., et al. 2025, *A&A*, 702, A211
- Lillo-Box, J., Lopez, T. A., Santerne, A., et al. 2020, *A&A*, 640, A48
- Lin, D. N. C., Bodenheimer, P., & Richardson, D. C. 1996, *Nature*, 380, 606
- Lopez, E. D. & Fortney, J. J. 2014, *ApJ*, 792, 1
- Lothringer, J. D., Rustamkulov, Z., Sing, D. K., et al. 2021, *ApJ*, 914, 12
- Lovis, C., Dumusque, X., Santos, N. C., et al. 2011, *arXiv e-prints*, arXiv:1107.5325
- MacDougall, M. G., Petigura, E. A., Fetherolf, T., et al. 2022, *AJ*, 164, 97
- Madhusudhan, N., Crouzet, N., McCullough, P. R., et al. 2014, *ApJ*, 791, L9
- Malavolta, L., Lovis, C., Pepe, F., Sneden, C., et al. 2017, *MNRAS*, 469, 3965
- Malavolta, L., Mayo, A. W., Louden, T., et al. 2018, *AJ*, 155, 107
- Malavolta, L., Nascimbeni, V., Piotto, G., et al. 2016, *A&A*, 588, A118
- Mamajek, E. E. & Hillenbrand, L. A. 2008, *ApJ*, 687, 1264
- Mann, A. W., Dupuy, T., Kraus, A. L., et al. 2019, *ApJ*, 871, 63
- Mantovan, G., Llancaqueo Alborno, A., Psaridi, A., et al. 2026, *arXiv e-prints*, arXiv:2605.04149
- Mantovan, G., Malavolta, L., Desidera, S., et al. 2024a, *A&A*, 682, A129
- Mantovan, G., Montalto, M., Piotto, G., et al. 2022, *MNRAS*, 516, 4432
- Mantovan, G., Wilson, T. G., Borsato, L., et al. 2024b, *A&A*, 691, A67
- McCully, C., Volgenau, N. H., Harbeck, D.-R., et al. 2018, in *Proc. SPIE*, Vol. 10707, 107070K
- McGurk, R., Rockosi, C., Gavel, D., et al. 2014, in *SPIE*, Vol. 9148, Adaptive Optics Systems IV, ed. E. Marchetti, L. M. Close, & J.-P. Vran, 91483A
- Mills, S. M., Howard, A. W., Weiss, L. M., et al. 2019, *AJ*, 157, 145
- Mollière, P., Wardenier, J. P., van Boekel, R., et al. 2019, *A&A*, 627, A67
- Mordasini, C., Alibert, Y., Benz, W., & Naef, D. 2008, in *Astronomical Society of the Pacific Conference Series*, Vol. 398, Extreme Solar Systems, ed. D. Fischer, F. A. Rasio, S. E. Thorsett, & A. Wolszczan, 235
- Murray, C. A. & Berta-Thompson, Z. 2025, *arXiv e-prints*, arXiv:2511.03045
- Mustill, A. J., Davies, M. B., & Johansen, A. 2015, *ApJ*, 808, 14
- Nabbie, E., Huang, C. X., Wittenmyer, R. A., & Zhou, G. 2026, *arXiv e-prints*, arXiv:2606.17218
- Naponiello, L., Mancini, L., Sozzetti, A., et al. 2023, *Nature*, 622, 255
- Nardiello, D., Malavolta, L., Desidera, S., et al. 2022, *A&A*, 664, A163
- Nardiello, D., Piotto, G., Deleuil, M., et al. 2020, *MNRAS*, 495, 4924
- Narita, N., Fukui, A., Kusakabe, N., et al. 2019, *Journal of Astronomical Telescopes, Instruments, and Systems*, 5, 015001
- Narita, N., Fukui, A., Yamamuro, T., et al. 2020, in *Society of Photo-Optical Instrumentation Engineers (SPIE) Conference Series*, Vol. 11447, SPIE, 114475K
- Nascimbeni, V., Borsato, L., Zingales, T., et al. 2023, *A&A*, 673, A42
- Nascimbeni, V., Piotto, G., Granata, V., et al. 2026, *arXiv e-prints*, arXiv:2604.03365
- Öberg, K. I., Murray-Clay, R., & Bergin, E. A. 2011, *ApJ*, 743, L16
- Osborn, A., Armstrong, D. J., Fernández Fernández, J., et al. 2023, *MNRAS*, 526, 548
- Pacetti, E., Turrini, D., Schisano, E., et al. 2022, *ApJ*, 937, 36
- Parviainen, H. 2016, *PyDE*: v1.5
- Parviainen, H. & Aigrain, S. 2015, *MNRAS*, 453, 3821
- Parviainen, H., Palle, E., Zapatero-Osorio, M. R., et al. 2020, *A&A*, 633, A28
- Pecaut, M. J. & Mamajek, E. E. 2013, *ApJS*, 208, 9
- Penzlin, A. B. T., Booth, R. A., Kirk, J., et al. 2024, *MNRAS*, 535, 171
- Pepe, F., Mayor, M., Galland, F., et al. 2002, *A&A*, 388, 632
- Pepe, F., Mayor, M., Rupprecht, G., et al. 2002, *The Messenger*, 110, 9
- Quinn, S. N., Rodriguez, J. E., Collins, K. A., et al. 2026, *AJ*, 171, 359
- Radzom, B. T., Dong, J., Rice, M., et al. 2025, *AJ*, 169, 189
- Rainer, M., Desidera, S., Borsa, F., et al. 2023, *A&A*, 676, A90
- Rajpaul, V., Aigrain, S., Osborne, M. A., et al. 2015, *MNRAS*, 452, 2269
- Ramírez, I., Meléndez, J., Bean, J., et al. 2014, *A&A*, 572, A48
- Rasio, F. A. & Ford, E. B. 1996, *Science*, 274, 954
- Rasmussen, C. E., Williams, C. K., et al. 2006, *Gaussian processes for machine learning*, Vol. 1 (Springer)
- Raymond, S. N., Mandell, A. M., & Sigurdsson, S. 2006, *Science*, 313, 1413
- Santos, N. C., Israelian, G., & Mayor, M. 2001, *A&A*, 373, 1019
- Santos, N. C., Israelian, G., & Mayor, M. 2004, *A&A*, 415, 1153
- Savel, A. B., Dressing, C. D., Hirsch, L. A., et al. 2020, *AJ*, 160, 287
- Schlaufman, K. C. & Winn, J. N. 2016, *ApJ*, 825, 62
- Schlegel, D. J., Finkbeiner, D. P., & Davis, M. 1998, *ApJ*, 500, 525
- Schwab, C., Rakich, A., Gong, Q., et al. 2016, in *Ground-Based and Airborne Instrumentation for Astronomy VI*, Vol. 9908 (SPIE), 2220–2225
- Scott, N. J., Howell, S. B., Horch, E. P., et al. 2018, *PASP*, 130, 054502
- Serrano, L. M., Gandolfi, D., Mustill, A. J., et al. 2022, *Nat. Astr.*, 6, 736
- Sha, L., Vanderburg, A. M., Huang, C. X., et al. 2023, *MNRAS*, 524, 1113
- Shappee, B. J., Prieto, J. L., Grupe, D., et al. 2014, *ApJ*, 788, 48
- Sousa, S. G., Santos, N. C., Adibekyan, V., et al. 2015, *A&A*, 577, A67
- Stassun, K. G., Collins, K. A., & Gaudi, B. S. 2017, *AJ*, 153, 136
- Stassun, K. G., Corsaro, E., Pepper, J. A., & Gaudi, B. S. 2018, *AJ*, 155, 22
- Stassun, K. G. & Torres, G. 2016, *AJ*, 152, 180
- Stassun, K. G. & Torres, G. 2021, *ApJ*, 907, L33
- Steffen, J. H., Fabrycky, D. C., Ford, E. B., et al. 2012, *MNRAS*, 421, 2342
- Storn, R. & Price, K. 1997, *Journal of Global Optimization*, 11, 341
- Sun, L., Ioannidis, P., Gu, S., et al. 2019, *A&A*, 624, A15
- Szentgyorgyi, A. H. & Fűrész, G. 2007, in *Rev. Mexicana Astron. Astrofis., ed. S. Kurtz*, Vol. 28, 129–133
- Turrini, D., Marzari, F., Polychroni, D., et al. 2023, *A&A*, 679, A55
- Visscher, C. & Moses, J. I. 2011, *ApJ*, 738, 72
- Wang, J., Xie, J.-W., Barclay, T., & Fischer, D. A. 2014, *ApJ*, 783, 4
- Wilson, T. G., Goffo, E., Alibert, Y., et al. 2022, *MNRAS*, 511, 1043
- Winn, J. N. 2010, in *Exoplanets*, ed. S. Seager, 55–77
- Wu, Y. & Murray, N. 2003, *ApJ*, 589, 605
- Zamyatina, M., Hébrard, E., Drummond, B., et al. 2023, *MNRAS*, 519, 3129
- Zechmeister, M. & Kürster, M. 2009, *A&A*, 496, 577
- Zeng, L., Jacobsen, S. B., Sasselov, D. D., et al. 2019, *PNAS*, 116, 9723

-
- ¹ Centro di Ateneo di Studi e Attività Spaziali “G. Colombo” – Università di Padova, Via Venezia 15, IT-35131, Padova, Italy; e-mail: giacomo.mantovan@unipd.it
 - ² Istituto Nazionale di Astrofisica - Osservatorio Astronomico di Padova, Vicolo dell’Osservatorio 5, IT-35122, Padova, Italy
 - ³ Dipartimento di Fisica e Astronomia “Galileo Galilei”, Università di Padova, Vicolo dell’Osservatorio 3, IT-35122, Padova, Italy
 - ⁴ Space Science and Astrobiology Division, NASA Ames Research Center, MS 245-3, Moffett Field, CA 94035, USA
 - ⁵ INAF - Osservatorio Astrofisico di Arcetri, Largo E. Fermi 5, 50125, Firenze, Italy
 - ⁶ INAF - Osservatorio Astronomico di Palermo, Piazza del Parlamento 1, I-90134, Palermo, Italy
 - ⁷ INAF - Osservatorio Astronomico di Trieste, Via Giambattista Tiepolo, 11, I-34131, Trieste (TS), Italy
 - ⁸ ESO - European Southern Observatory, Alonso de Córdova 3107, Casilla 19, Santiago, 19001, Chile
 - ⁹ INAF – Osservatorio Astronomico di Roma, Via Frascati 33, 00078, Monte Porzio Catone (Roma), Italy
 - ¹⁰ Center for Astrophysics | Harvard & Smithsonian, 60 Garden Street, Cambridge, MA 02138, USA
 - ¹¹ INAF – Osservatorio Astrofisico di Torino, Via Osservatorio 20, IT-10025, Pino Torinese, Italy
 - ¹² Komaba Institute for Science, The University of Tokyo, 3-8-1 Komaba, Meguro, Tokyo 153-8902, Japan
 - ¹³ NSF NOIRLab, 950 N. Cherry Ave., Tucson, AZ 85719, USA
 - ¹⁴ Dipartimento di Fisica, Università degli Studi di Torino, via Pietro Giuria 1, I-10125, Torino, Italy
 - ¹⁵ Department of Astronomy, California Institute of Technology, Pasadena, CA 91125, USA
 - ¹⁶ INAF - Osservatorio Astrofisico di Catania, Oss. Astr. Catania, via S. Sofia 78, 95123 Catania Italy
 - ¹⁷ Department of Physics and Astronomy, Vanderbilt University, Nashville, TN 37235, USA
 - ¹⁸ Department of Physics & Astronomy, University of California Los Angeles, Los Angeles, CA 90095, USA
 - ¹⁹ Department of Astronomy, University of California, Berkeley, Berkeley, CA 94720, USA
 - ²⁰ Instituto de Astrofísica de Canarias (IAC), 38205 La Laguna, Tenerife, Spain
 - ²¹ Fundación Galileo Galilei – INAF, Rambla José Ana Fernández Pérez 7, 38712 Breña Baja, TF, Spain
 - ²² Graduate School of Social Data Science, Hitotsubashi University, 2-1 Naka, Kunitachi, Tokyo 186-8601, Japan
 - ²³ Department of Physical Sciences, Ritsumeikan University, Kusatsu, Shiga 525-8577, Japan
 - ²⁴ Lund Observatory, Division of Astrophysics, Department of Physics, Lund University, Box 118, 22100 Lund, Sweden
 - ²⁵ Departamento de Astrofísica, Universidad de La Laguna (ULL), E-38206 La Laguna, Tenerife, Spain
 - ²⁶ Dipartimento di Fisica, Università di Roma Tor Vergata, Via della Ricerca Scientifica 1, 00133, Roma, Italy

²⁷ Max Planck Institute for Astronomy, Königstuhl 17, 69117, Heidelberg, Germany

²⁸ Astrobiology Center, 2-21-1 Osawa, Mitaka, Tokyo 181-8588, Japan

²⁹ National Astronomical Observatory of Japan, 2-21-1 Osawa, Mitaka, Tokyo 181-8588, Japan

³⁰ Department of Astronomy, University of Maryland, College Park, College Park, MD 20742, USA

³¹ Department of Physics and Kavli Institute for Astrophysics and Space Research, Massachusetts Institute of Technology, Cambridge, MA 02139, USA

³² Kotizarovci Observatory, Sarsoni 90, 51216 Viskovo, Croatia

³³ Hazelwood Observatory, Australia

³⁴ Planetary Discoveries, Valencia, CA 91354, USA

³⁵ Società Astronomica Lunae, Castelnuovo Magra, Italy

Appendix A: Detailed stellar activity modelling

Our corrected *TESS* light curve for sector 85 displayed significant instrumental variability (mainly stray light). This behaviour often occurred when the photometry was associated with high local background values and forced us to mask these points, making it impossible to get a complete, well-detrended light curve. This impacted our ability to preserve the stellar variability and hence model its short-term properties precisely.

For this reason, and also because the zero point with respect to sector 84 was challenging to retrieve, we decided not to use *TESS* sector 85 as one of the observables in the multidimensional GP. Nevertheless, we included it in our joint fit and modelled it using a unidimensional GP that shared the stellar rotation period (a rather long-term property) with the multidimensional GP, as done for the other *TESS* sectors.

When we initially attempted to include sector 85 as an observable in the multidimensional GP framework, the Bayesian analysis failed to converge. The reason for this outcome was the difficulty of finding a set of hyperparameters that could consistently explain sector 85 (and its instrumental variability) plus all other *TESS* sectors and activity indicators.

Appendix B: Dynamical analysis

The retrieved transit times (T_0) of TOI-1533 b and TOI-1533 c were modelled by numerically integrating the system with the N-body integrator TRADES. We adopted the same fitting framework, the same analysis procedure (PyDE exploration, emcee sampling, and convergence criteria) described in Leonardi et al. (2025). Specifically, we used an integration time (T_{int}) of 2506 days that covers the entire observation time span, and a time start of the integration $T_{\text{ref, dyn}} = 2458760.0 \text{ BJD}_{\text{TDB}}$.

This analysis successfully retrieved planetary parameters that are consistent with those reported in Table 2. However, there is still a significant scatter in the residuals of both O-C diagrams. The most likely source of this scatter is in-transit stellar activity affecting the *TESS* light-curves. TTVs of about 10 minutes could be explained by the presence of stellar spots (e.g. Murray & Berta-Thompson 2025), but these could only be modelled out of the transits with exquisite, high-precision photometry, such as CHEOPS.

Appendix C: Independent stellar parameters determination

As an independent determination of the basic stellar parameters, we performed an analysis of the broadband spectral energy distribution (SED) of the star together with the *Gaia* DR3 parallax (with no systematic offset applied; see, e.g., Stassun & Torres 2021), to determine an empirical measurement of the stellar radius, following the procedures described in Stassun & Torres (2016); Stassun et al. (2017, 2018). We pulled the JHK_S magnitudes from *2MASS*, the $G_{\text{BP}}G_{\text{RP}}$ magnitudes from *Gaia*, and the W1–W4 magnitudes from *WISE*. We also utilised the absolute flux-calibrated spectrophotometry from *Gaia*. Together, the available photometry spans the full stellar SED over the wavelength range 0.4–20 μm (see Figure C.1).

We performed a fit using PHOENIX stellar atmosphere models (Husser et al. 2013b), with the effective temperature (T_{eff}), surface gravity ($\log g$), and metallicity ($[\text{Fe}/\text{H}]$) adopted from the spectroscopic analysis. The extinction, A_V , was limited to the maximum line-of-sight value from the Galactic dust maps

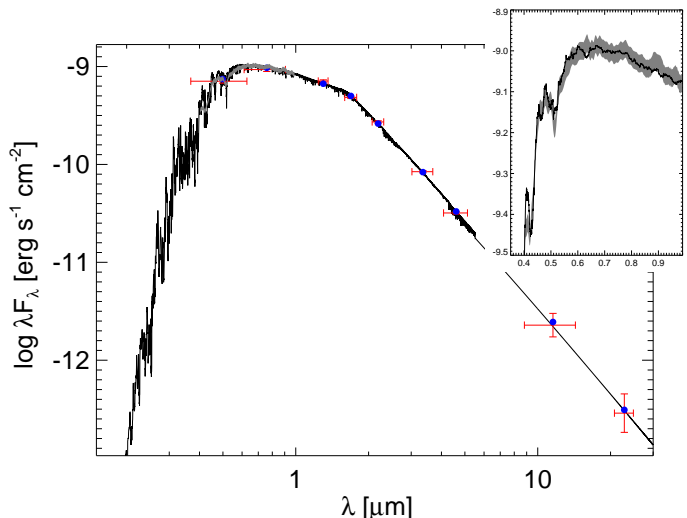


Fig. C.1: Spectral energy distribution of TOI-1533. Red symbols represent the observed photometric measurements, where the horizontal bars represent the effective width of the passband. Blue symbols are the model fluxes from the best-fit PHOENIX atmosphere model (black). The *Gaia* spectrophotometry is overlaid as the grey swathe, also in the inset plot.

of Schlegel et al. (1998). The resulting fit (Figure C.1) has a reduced χ^2 of 1.5, with a best-fit $A_V = 0.01 \pm 0.01$. Integrating the (unreddened) model SED gives the bolometric flux at Earth, $F_{\text{bol}} = 1.396 \pm 0.016 \times 10^{-9} \text{ erg s}^{-1} \text{ cm}^{-2}$. Taking the F_{bol} together with the *Gaia* parallax directly gives the bolometric luminosity, $L_{\text{bol}} = 0.4349 \pm 0.0051 L_{\odot}$. The stellar radius follows from the Stefan-Boltzmann relation, giving $R_{\star} = 0.837 \pm 0.024 R_{\odot}$. In addition, we can estimate the stellar mass from the empirical relations of Mann et al. (2019), giving $M_{\star} = 0.82 \pm 0.04 M_{\odot}$.

Appendix D: Further atmospheric follow-up prospects

The expected day-to-night temperature contrasts (Komacek & Showman 2016) induce longitudinal chemical gradients (Zamyatina et al. 2023), leading to compositional asymmetries between the eastern and western limbs (Espinoza et al. 2024), given the equilibrium temperature of this planet. However, the grazing nature of the transit makes TOI-1533 c a challenging target to interpret. The transit geometry reduces the effective atmospheric annulus probed in transmission and limits the fraction of the terminator that is sampled. At the same time, this partial sampling presents a unique opportunity, as it may enhance sensitivity to localised atmospheric regions rather than averaging uniformly over the full limb. Such a geometry could enable novel constraints on wind patterns and limb asymmetries, particularly when combined with ground-based high-resolution spectroscopy capable of resolving Doppler-shifted molecular lines. Measurements of line shifts and broadening could, in principle, isolate contributions from specific regions of the terminator. However, the lack of constraints on the planet's three-dimensional orientation and obliquity complicates the interpretation of the observed spectra through transmission spectroscopy. Although difficult, a detailed atmospheric characterisation of this system would provide a rare opportunity to link disk chemistry, dynamical evolution, and present-day atmospheric composition within a single planetary architecture.

Table E.1: List of systems presented in this work.

System	Class ^a	Discovery paper	Parameters paper
WASP-47	H	Becker et al. (2015)	Nascimbeni et al. (2023)
TOI-1408	H	Korth et al. (2024)	Same as discovery
TOI-5143	H	Radzom et al. (2025)	/
Kepler-730	H	Cañas et al. (2019)	/
WASP-132	H	Hord et al. (2022)	Grieves et al. (2025)
Kepler-18	IM	Cochran et al. (2011)	Same as discovery
Kepler-411	IM	Wang et al. (2014)	Sun et al. (2019)
K2-19	IM	Barros et al. (2015)	Almenara et al. (2025)
TOI-1533	IM	This work	This work
TOI-1130	H	Huang et al. (2020)	Borsato et al. (2024)
TOI-1272	IM	MacDougall et al. (2022)	Same as discovery
K2-32	IM	Dai et al. (2016)	Lillo-Box et al. (2020)
TOI-2000	H, IM	Sha et al. (2023)	Same as discovery
TOI-5398	H, IM	Mantovan et al. (2022)	Mantovan et al. (2024a)
CoRoT-24	IM	Alonso et al. (2014)	Same as discovery
Kepler-25	IM	Steffen et al. (2012)	Mills et al. (2019)
TOI-4010	IM	Kunimoto et al. (2023)	Same as discovery
Kepler-9	IM	Holman et al. (2010)	Borsato et al. (2019)

Notes. ^(a) System class: H stands for ‘Hot giant’ and IM stands for ‘intermediate-mass’ planet.

Appendix E: Hot giants and intermediate-mass planets with inner companions

Appendix F: Extra figures and tables

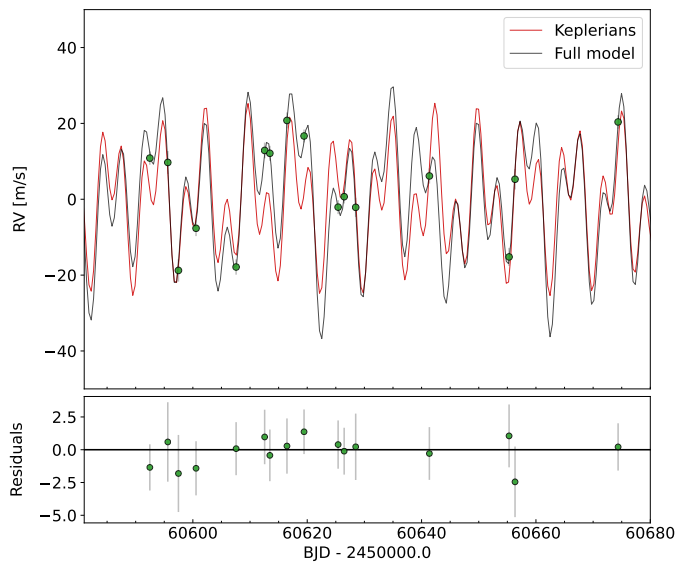


Fig. F.1: Modelling of HARPS-N RV time series. *Top*: RV time series with superimposed full Keplerian + stellar activity model (black line), and full Keplerian only (red line). *Bottom*: Residuals of the fit.

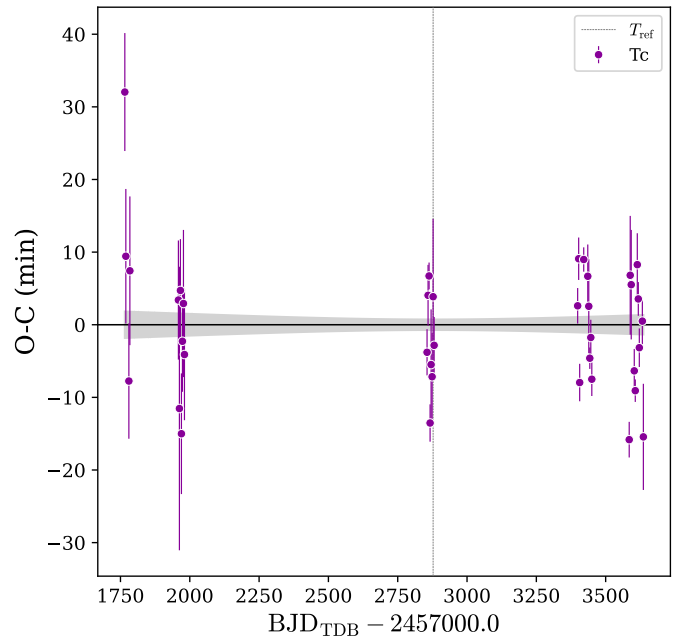


Fig. F.2: Observed minus calculated transit times for the linear ephemeris of TOI-1533 b. The grey area shows the formal uncertainty of the linear ephemeris.

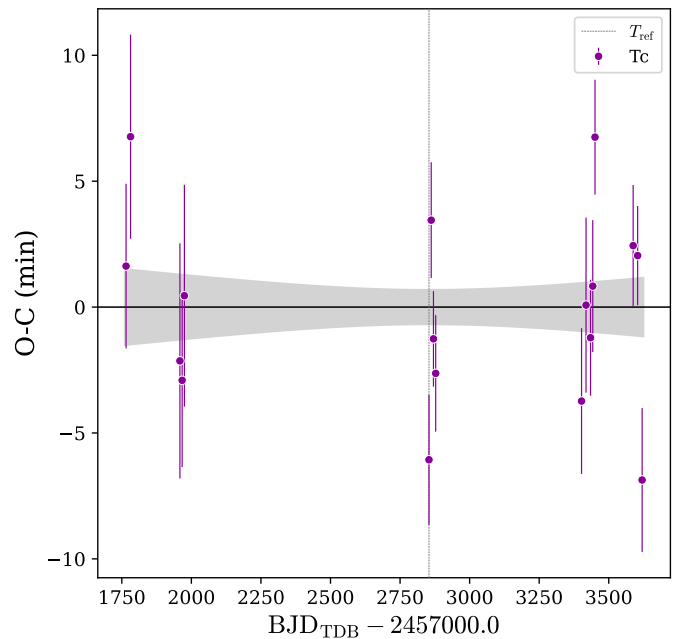


Fig. F.3: Same as in figure F.2 but for planet TOI-1533 c.

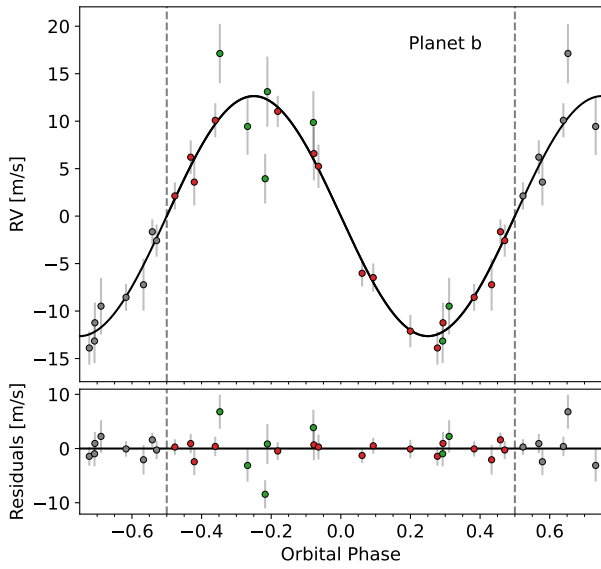


Fig. F.4: Phase-folded RV curve of TOI-1533 b with NEID RVs included. The different colours represent different datasets: red for HARPS-N and green for NEID. The residuals of the fit are shown in the *bottom* panel.

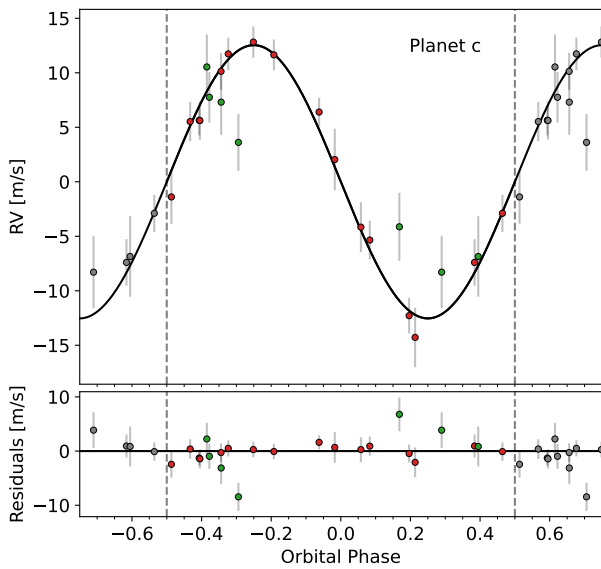


Fig. F.5: Same as in figure F.4 but for planet TOI-1533 c.

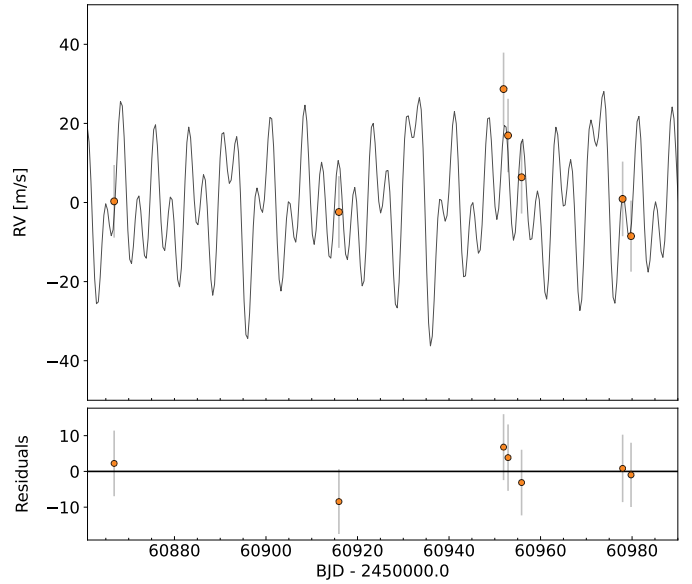


Fig. F.6: Same as in figure F.1 but for NEID data.

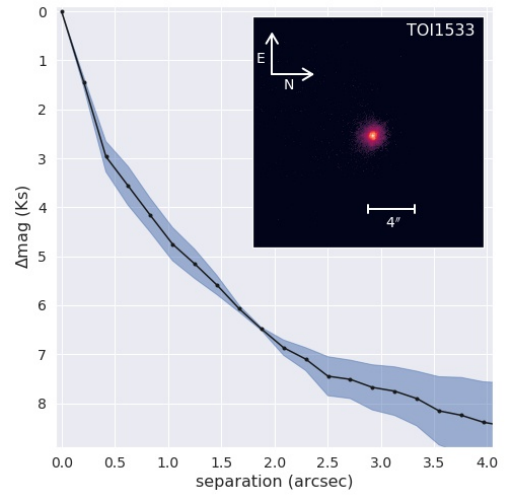


Fig. F.7: Adaptive optics images of TOI-1533 taken with the ShARCS camera. We also present a contrast curve generated by calculating the median values (solid lines) and root-mean-square errors (blue, shaded regions) in annuli centred on each target, where the bin width of each annulus is equal to the full width at half max of the point spread function.

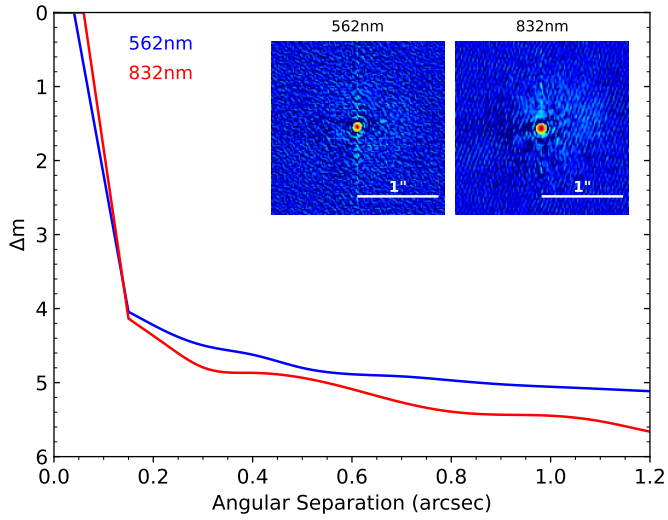


Fig. F.8: Contrast curves for TOI-1533 at 562 nm (blue) and 832 nm (red) obtained from NESSI speckle imaging. Reconstructed images are shown as insets to the plot with wavelengths labelled. Here, North is toward the top and East to the left.

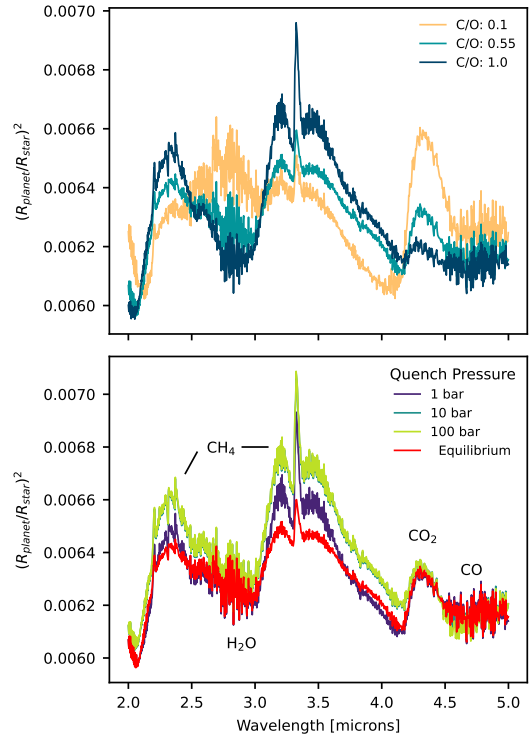


Fig. F.10: Simulated transmission spectrum of TOI-1533 c generated with petitRADTRANS (Mollière et al. 2019) using the planetary parameters reported in this work and a Guillot temperature–pressure profile (Guillot 2010, $\kappa_{\text{IR}} = 0.05$, $\gamma = 0.1$, and $T_{\text{int}} = 100$ K). Top panel: Spectra for different atmospheric carbon-to-oxygen (C/O) ratios. Bottom panel: Comparison between chemical equilibrium and disequilibrium models with varying quench pressures, assuming C/O = 0.55.

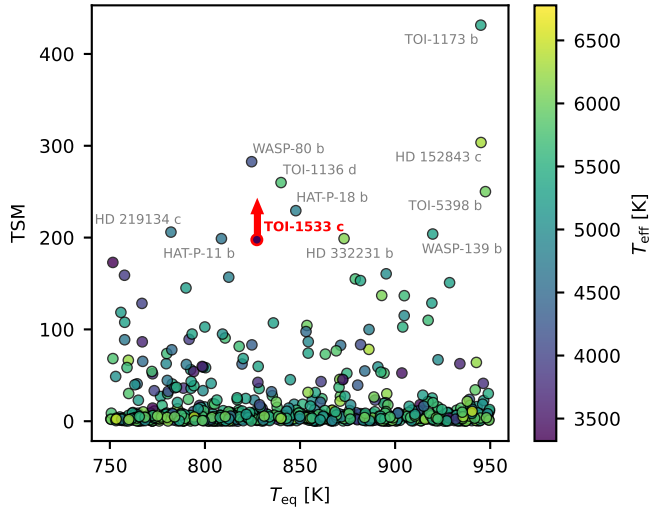


Fig. F.9: TSM for planets with equilibrium temperatures between 750 and 850 K. TOI-1533 c is highlighted in red, its TSM is computed assuming the minimum reported planetary radius. Points are colour-coded by the effective temperature of the host star. Planetary and stellar parameters are taken from the NASA Exoplanet Archive (Christiansen et al. 2025).

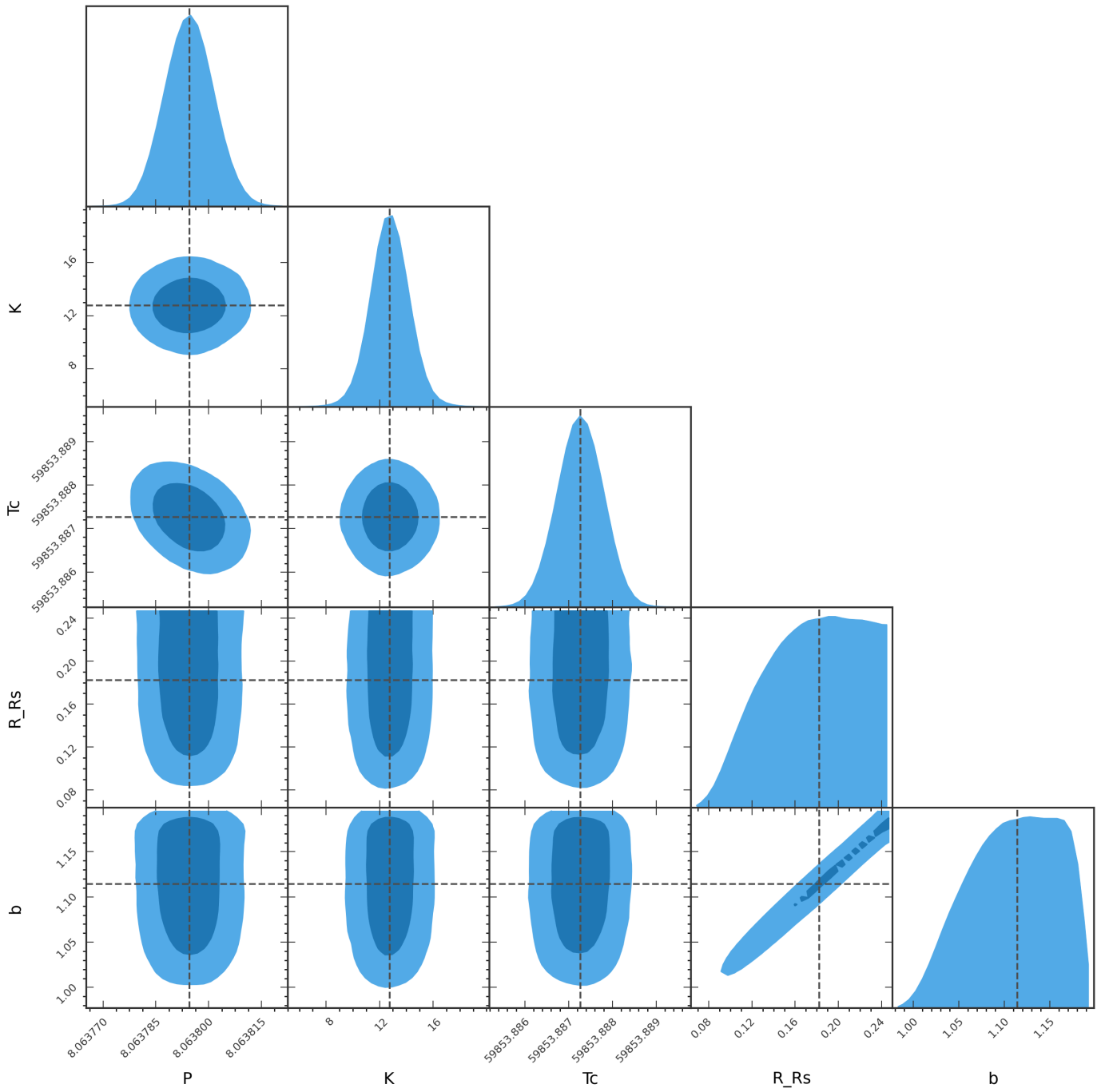


Fig. F.11: Posterior distributions of TOI-1533 c transit model fit.

Table F.1: Priors and outcomes of full modelling.

Parameter	Unit	Prior	Value
<i>TESS</i> s17 jitter (σ_{jitter}^{s17})	ppt	...	0.29±0.01
<i>TESS</i> s24 jitter (σ_{jitter}^{s24})	ppt	...	0.34±0.02
<i>TESS</i> s57 jitter (σ_{jitter}^{s57})	ppt	...	0.19±0.01
<i>TESS</i> s77 jitter (σ_{jitter}^{s77})	ppt	...	0.12±0.02
<i>TESS</i> s78 jitter (σ_{jitter}^{s78})	ppt	...	0.26 ^{+0.03} _{-0.02}
<i>TESS</i> s84 jitter (σ_{jitter}^{s84})	ppt	...	0.23±0.02
<i>TESS</i> s85 jitter (σ_{jitter}^{s85})	ppt	...	0.15±0.02
<i>MuSCAT2</i> jitter ($\sigma_{jitter}^{MuSCAT2}$)	ppt	...	0.32±0.20
Teide 23/12/03 jitter (σ_{jitter}^{Teide})	ppt	...	0.53±0.10
Teide 24/08/04 jitter (σ_{jitter}^{Teide})	ppt	...	0.53±0.13
Teide 24/08/11 jitter (σ_{jitter}^{Teide})	ppt	...	1.16±0.10
Hal 23/10/07 jitter (σ_{jitter}^{Hal})	ppt	...	1.40±0.18
Hal 24/10/12 jitter (σ_{jitter}^{Hal})	ppt	...	0.81±0.07
Hal 25/11/03 jitter (σ_{jitter}^{Hal})	ppt	...	0.65±0.04
Uncorr. RHK jitter (σ_{jitter}^{RHK})		...	0.004 ^{+0.004} _{-0.003}
Uncorr. FWHM jitter	km s ⁻¹	...	0.002±0.002
RHK offset (γ^{RHK})		...	-4.49 ^{+0.01} _{-0.02}
FWHM offset (γ^{FWHM})	km s ⁻¹	...	6.74 ^{+0.01} _{-0.02}
<i>TESS</i> quad. LD coeff. (u_1)		$\mathcal{U}(0, 1)$	0.38 ^{+0.33} _{-0.26}
<i>TESS</i> quad. LD coeff. (u_2)		$\mathcal{U}(0, 1)$	0.24 ^{+0.30} _{-0.38}
<i>MuSCAT2</i> i' LD (u_1)		$\mathcal{N}(0.50, 0.10)$	0.54±0.08
<i>MuSCAT2</i> i' LD (u_2)		$\mathcal{N}(0.11, 0.11)$	0.16±0.09
<i>LCO Sinistro</i> z_s LD (u_1)		$\mathcal{N}(0.42, 0.10)$	0.43±0.09
<i>LCO Sinistro</i> z_s LD (u_2)		$\mathcal{N}(0.12, 0.11)$	0.13±0.10
<i>MuSCAT3</i> g' LD (u_1)		$\mathcal{N}(0.84, 0.10)$	0.82 ^{+0.07} _{-0.08}
<i>MuSCAT3</i> g' LD (u_2)		$\mathcal{N}(-0.02, 0.11)$	-0.04 ^{+0.09} _{-0.08}
<i>GP parameters</i>			
Rot _{Q0}		...	0.78 ^{+0.55} _{-0.32}
Rot _{deltaQ}		...	0.0001 ^{+0.08} _{-0.0001}
Rot _{fmix}		...	0.128 ^{+0.25} _{-0.099}
Rot _{σ} s17		...	0.0064 ^{+0.002} _{-0.001}
Rot _{σ} s24		...	0.0058 ^{+0.0012} _{-0.0009}
Rot _{σ} s57		...	0.0062 ^{+0.0011} _{-0.0009}
Rot _{σ} s77		...	0.0033 ^{+0.0007} _{-0.0005}
Rot _{σ} s78		...	0.014 ^{+0.003} _{-0.002}
Rot _{σ} s85		...	0.009±0.002
V_c (RV)	m s ⁻¹	$\mathcal{U}(0, 40)$	5.8 ^{+2.1} _{-1.5}
V_r (RV)	m s ⁻¹	$\mathcal{U}(-40, 40)$	18.3 ^{+5.8} _{-4.3}
$L2_c$ (RHK)		$\mathcal{U}(-0.5, 0.5)$	0.032 ^{+0.010} _{-0.007}
$L3_c$ (Flux)	ppt	$\mathcal{U}(-1000, 1000)$	-6 ⁺¹ ₋₂
L_c (FWHM)	km s ⁻¹	$\mathcal{U}(-0.2, 0.2)$	0.033 ^{+0.010} _{-0.006}